

Shallow Tectonic Stress Magnitudes at the Hikurangi Subduction Margin, New Zealand

Effat Behboudi¹, David Daniel McNamara², and Ivan Lokmer³

¹School of Earth Sciences

²University of Liverpool

³University College Dublin

December 22, 2022

Abstract

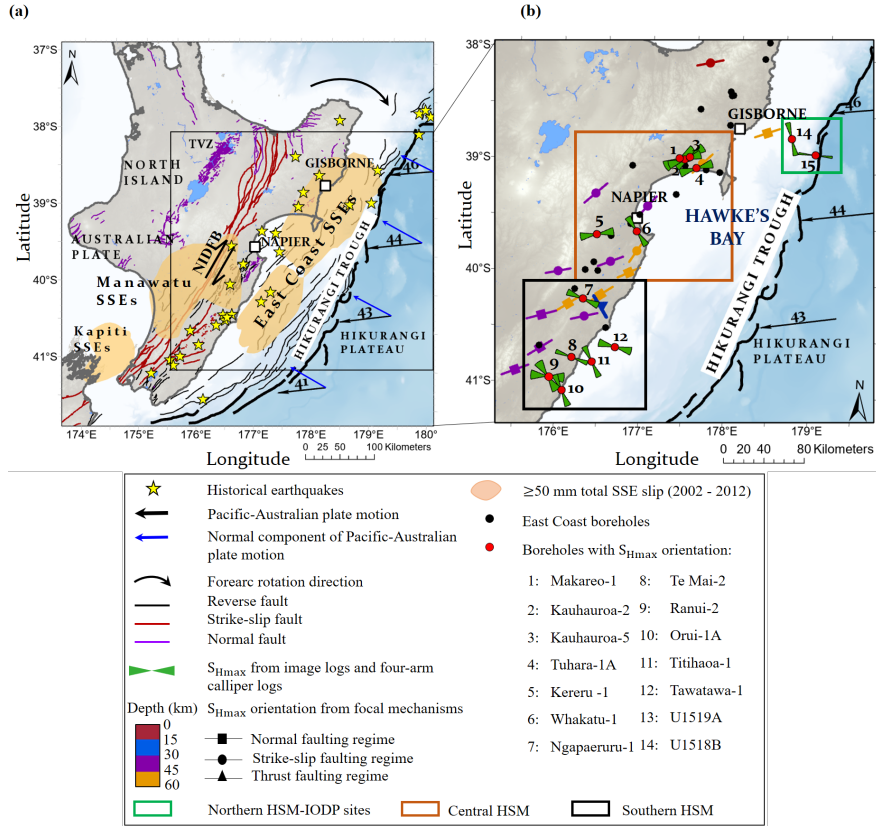
Quantifying tectonic stress magnitudes is crucial in understanding crustal deformation processes, fault geomechanics, and variable plate interface slip behaviors in subduction zones. The Hikurangi Subduction Margin (HSM), New Zealand is characterized by along-strike variation in interface slip behavior, which may be linked to tectonic stress variations within the overriding plate. This study constrains in-situ stress magnitudes of the shallow (<3km) overriding plate of the HSM to better understand its tectonics and how they relate to larger scale subduction dynamics. Results reveal σ_3 : S_v ratios of 0.6-1 at depths above 650-700 m TVD and 0.92-1 below this depth interval along the HSM and SHmax: S_v ratios of 0.95-1.81 in the central HSM, and 0.95-3.12 in the southern HSM. These stress ratios suggest a prevalent thrust to strike-slip ($\sigma_1=SHmax$) faulting regime across the central and southern HSM. In the central HSM, the presence of NNE-NE striking reverse faults co-existing with a modern σ_1 aligned ENE-WSW (SHmax) suggests that overtime the stress state here evolved from a contractional to a strike-slip state, where the compressional direction changes from perpendicular (NW-SE) to subparallel (ENE-WSW) to the Hikurangi margin. This temporal change in stress state may be explained by forearc rotation, likely combined with development of upper plate overpressures. In the southern HSM, the modern WNW-ESE/ NW-SE σ_1 (SHmax) and pre-existing NNE-NE striking reverse faults indicate that stress state remains contractional and subparallel (NW-SE) to the Hikurangi margin overtime. This may reflect the interseismic locked nature of the plate interface.

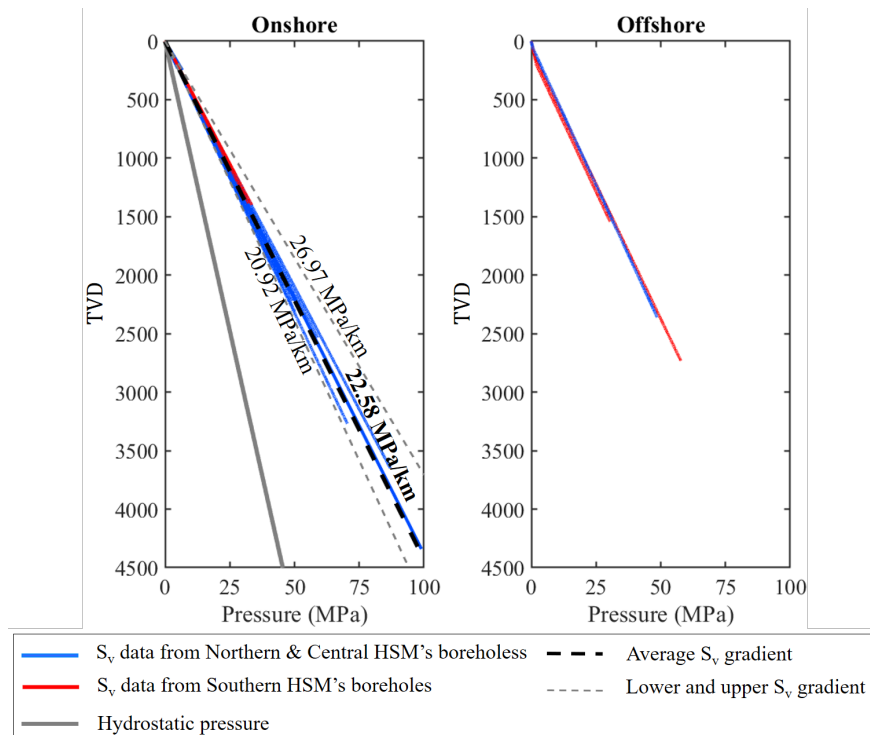
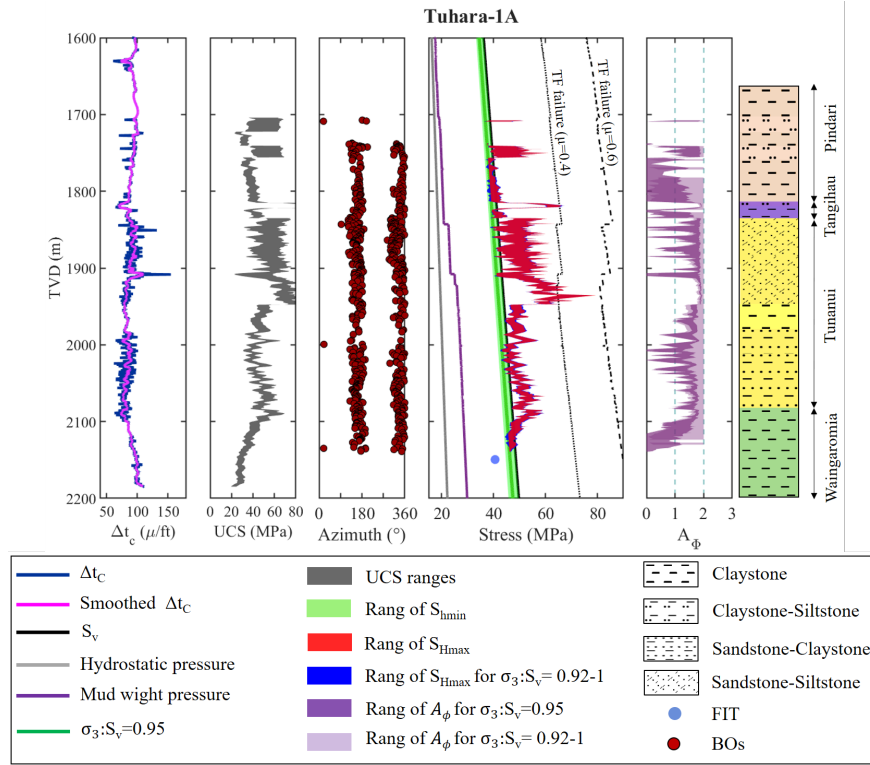
Hosted file

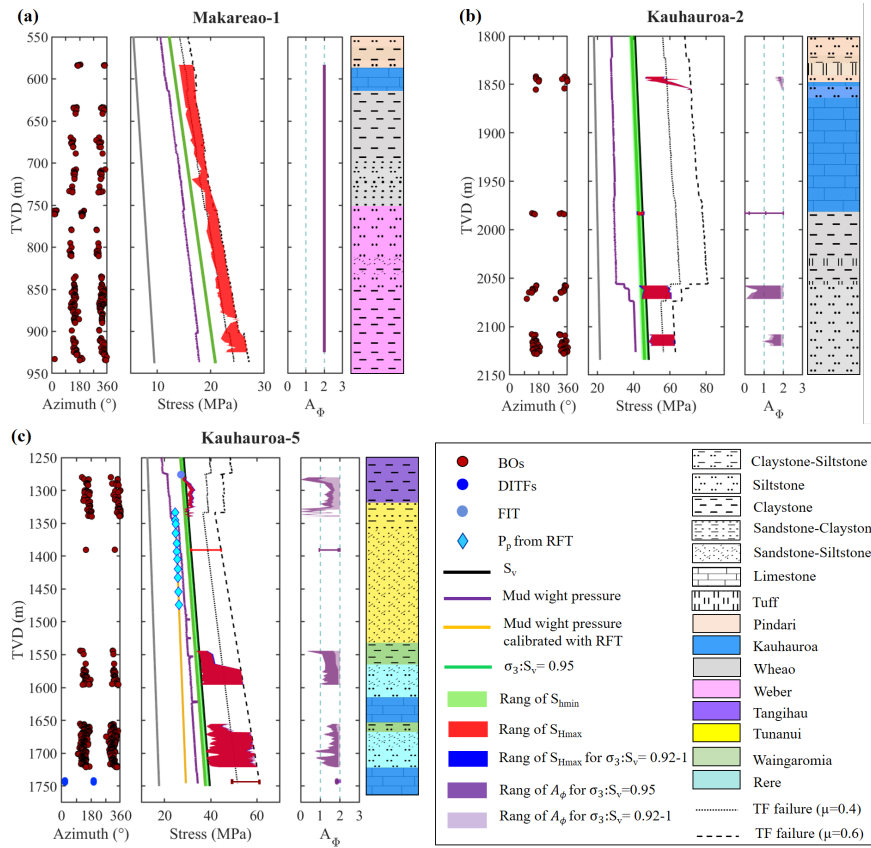
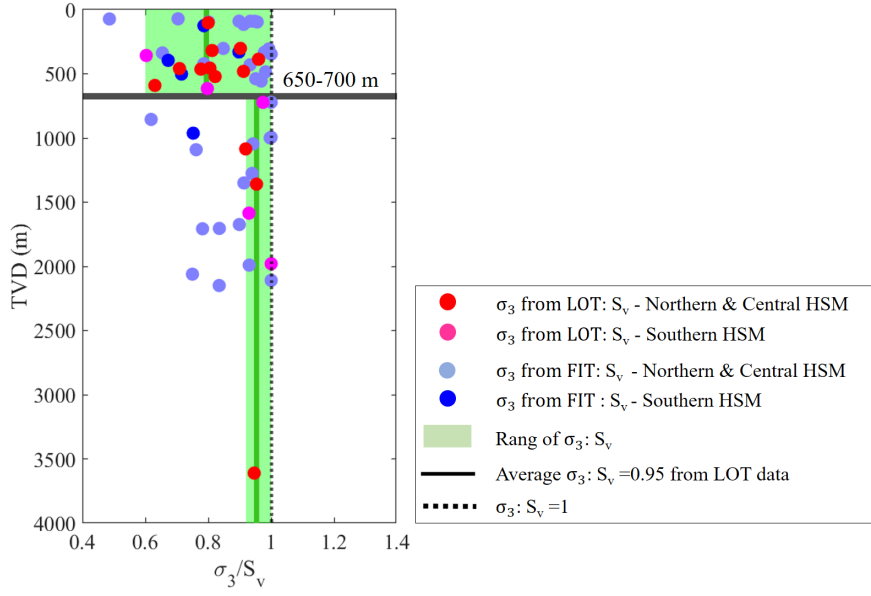
952355_0_art_file_10544524_rn7mj1.docx available at <https://authorea.com/users/531433/articles/614577-shallow-tectonic-stress-magnitudes-at-the-hikurangi-subduction-margin-new-zealand>

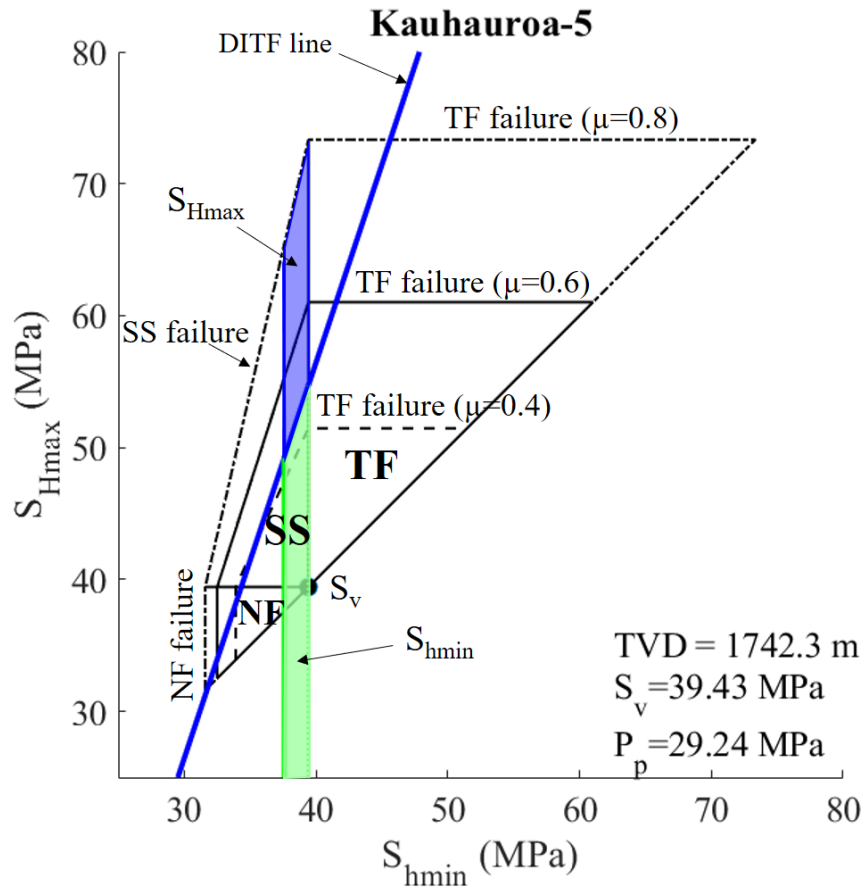
Hosted file

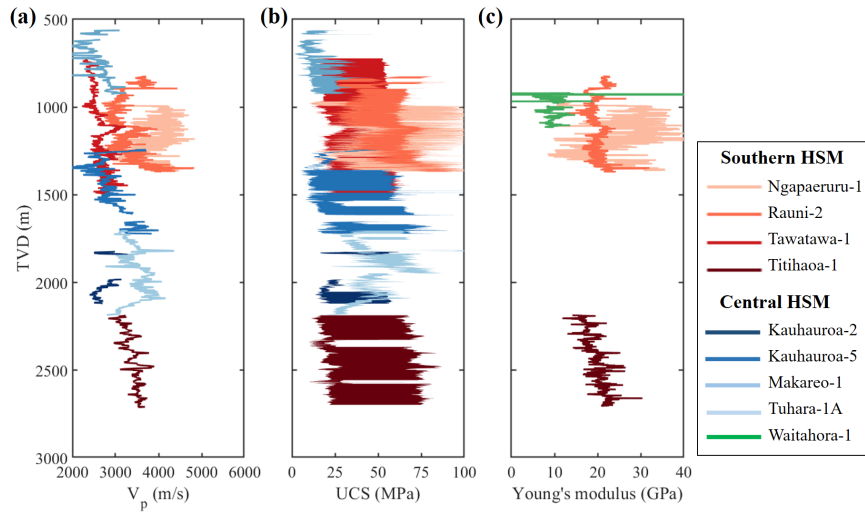
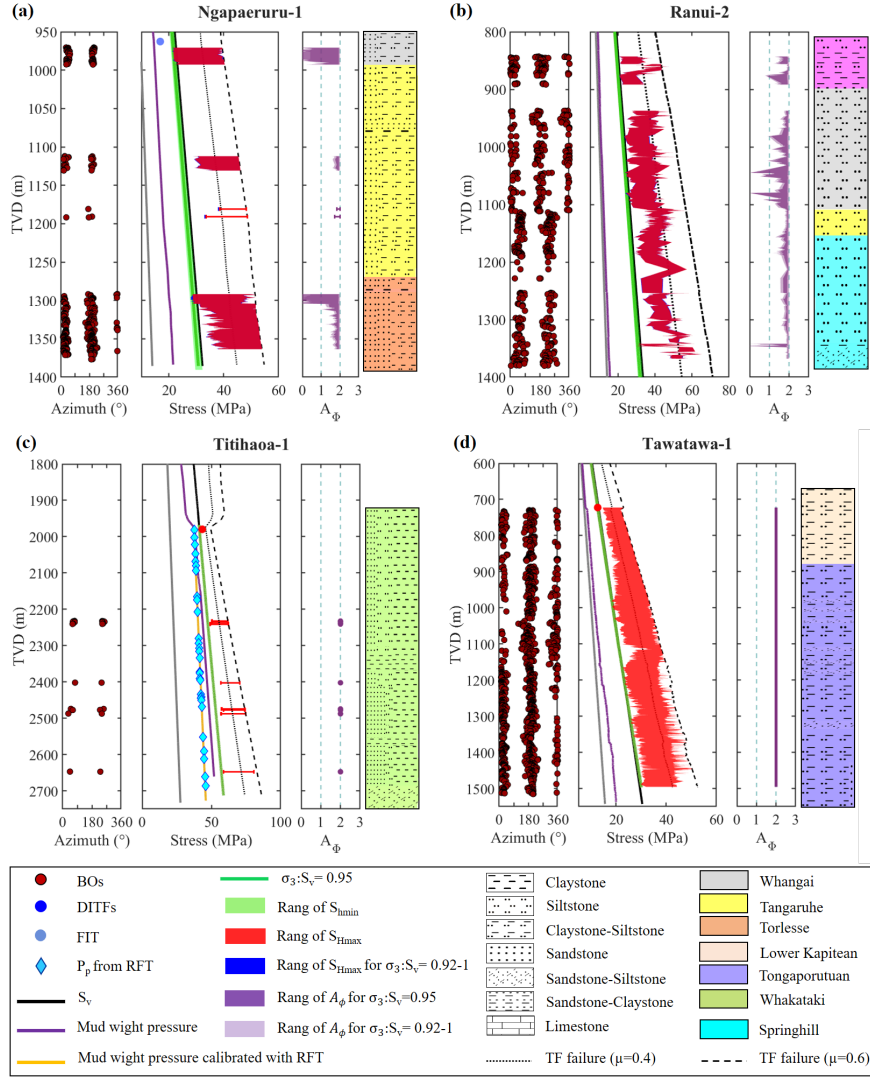
952355_0_supp_10544561_rn13zh.docx available at <https://authorea.com/users/531433/articles/614577-shallow-tectonic-stress-magnitudes-at-the-hikurangi-subduction-margin-new-zealand>

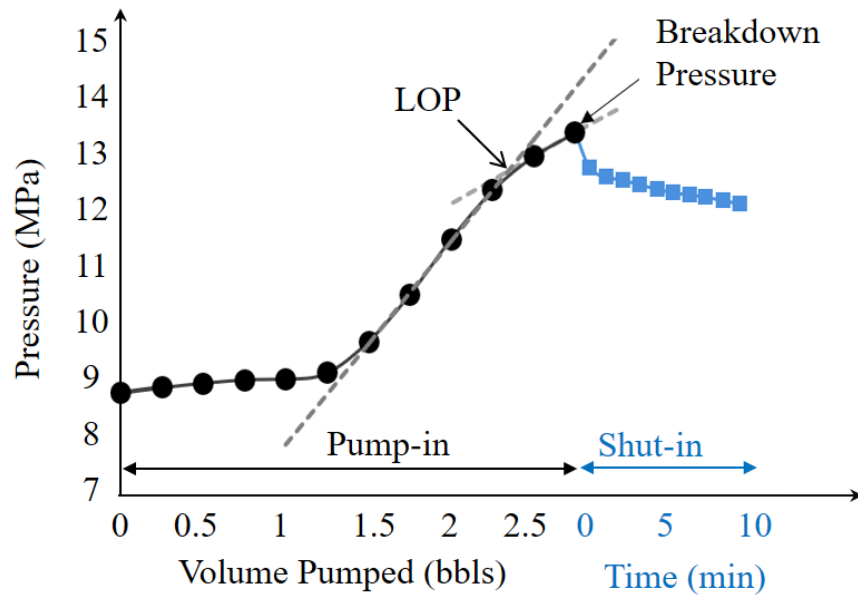


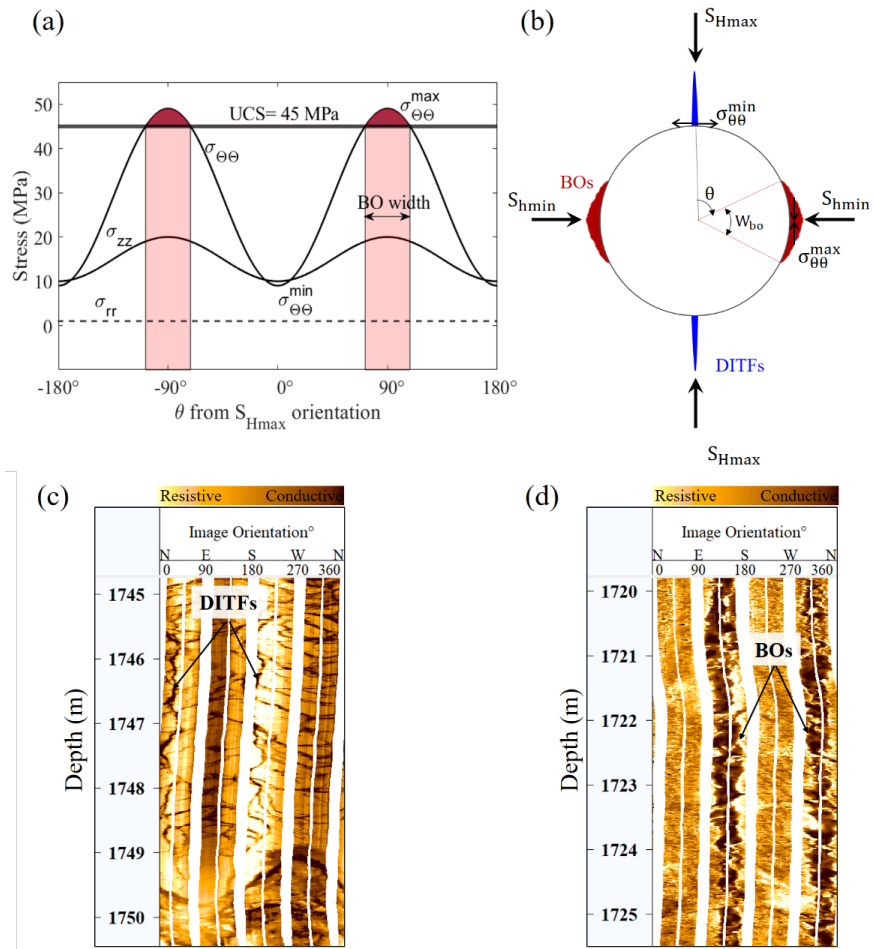












1 **Shallow Tectonic Stress Magnitudes at the Hikurangi Subduction**
2 **Margin, New Zealand**

3
4 **E. Behboudi^{1,2}, D.D. McNamara³, I. Lokmer^{1,2}**

5 ¹ Irish Centre for Applied Geosciences (iCRAG), University College Dublin, Republic of
6 Ireland.

7 ² School of Earth Sciences, University College Dublin, Republic of Ireland.

8 ³ Department of Earth, Ocean and Ecological Sciences, University of Liverpool, UK.

9

10 Corresponding author: Effat Behboudi (effat.behboudi@ucdconnect.ie)

11

12

13

14

15

16

17

18

19

20

21

22

23

24

25

26

27

28

29

30

31

32

33

34

35

36 **Abstract**

37 Quantifying tectonic stress magnitudes is crucial in understanding crustal deformation
38 processes, fault geomechanics, and variable plate interface slip behaviors in subduction
39 zones. The Hikurangi Subduction Margin (HSM), New Zealand is characterized by along-
40 strike variation in interface slip behavior, which may be linked to tectonic stress variations
41 within the overriding plate. This study constrains *in-situ* stress magnitudes of the shallow
42 (<3km) overriding plate of the HSM to better understand its tectonics and how they relate to
43 larger scale subduction dynamics. Results reveal $\sigma_3: S_v$ ratios of 0.6-1 at depths above 650-
44 700 m TVD and 0.92-1 below this depth interval along the HSM and $S_{Hmax}: S_v$ ratios of 0.95-
45 1.81 in the central HSM, and 0.95-3.12 in the southern HSM. These stress ratios suggest a
46 prevalent thrust to strike-slip ($\sigma_1=S_{Hmax}$) faulting regime across the central and southern
47 HSM. In the central HSM, the presence of NNE-NE striking reverse faults co-existing with a
48 modern σ_1 aligned ENE-WSW (S_{Hmax}) suggests that overtime the stress state here evolved
49 from a contractional to a strike-slip state, where the compressional direction changes from
50 perpendicular (NW-SE) to subparallel (ENE-WSW) to the Hikurangi margin. This temporal
51 change in stress state may be explained by forearc rotation, likely combined with
52 development of upper plate overpressures. In the southern HSM, the modern WNW-ESE/
53 NW-SE σ_1 (S_{Hmax}) and pre-existing NNE-NE striking reverse faults indicate that stress state
54 remains contractional and subparallel (NW-SE) to the Hikurangi margin overtime. This may
55 reflect the interseismic locked nature of the plate interface.

56 **Plain Language Summary**

57 The type of geological faults and their movement are partially controlled by forces generated
58 from plate movement, known as *in-situ* stress. This stress state can also be changed overtime
59 due to the occurrence of earthquakes on such faults. The HSM is New Zealand's largest and
60 most hazardous plate boundary fault and experiences different types of earthquakes that may
61 be related to variations in *in-situ* stress of the plates involved in this subduction boundary.
62 This study quantifies for the first time the stresses associated with the modern HSM, and
63 finds that they and their resulting tectonic behavior have changed with geological time in the
64 central regions. This change is likely related to the effects of other nearby tectonic processes
65 further inland and to the development of high pore pressures in the overriding plate in this
66 region.

67 **Key Points**

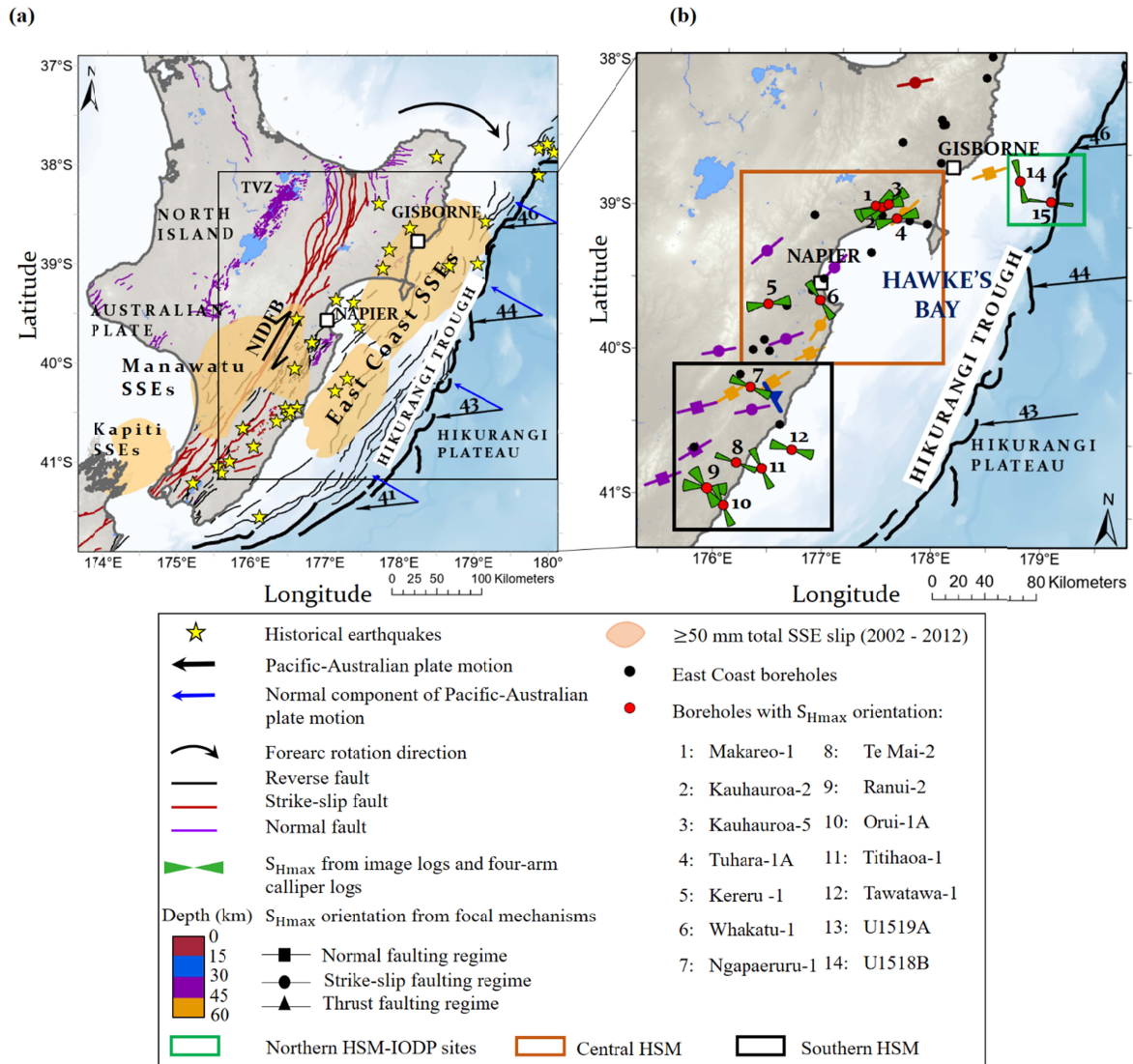
- 68 • For the shallow crust (upper 3 km) of the Hikurangi Subduction Margin, $\sigma_1 = S_{Hmax}$.
- 69 • σ_1 rotates from margin-parallel (NW-SE) to margin-perpendicular (WNW-ESE) in the
70 central Hikurangi Subduction Margin overtime.
- 71 • The shift in the stress state overtime in the central HSM may be driven by forearc rotation
72 and shallow overpressures in this region.
- 73 • σ_1 remains perpendicular (NW-SE/WNW-ESE) to the margin overtime in the southern
74 HSM, may reflect the interseismic locked nature of the plate interface.

75 **1 Introduction**

76 Large magnitude, tsunamigenic earthquakes commonly occur at subduction plate boundaries
77 and are associated with a wide range of tectonic fault slip behaviors along the subduction
78 interface including slow slip events (SSEs), low-frequency earthquakes (LFES), very-low-
79 frequency earthquakes (VLFES), and episodic tremor and slip (ETS) (Audet et al., 2009; Ito
80 & Obara, 2006; Kodaira et al., 2004; Liu & Rice, 2007; Ujiie & Kimura, 2014). Earthquake
81 occurrence such as nucleation of earthquake ruptures and rupture propagations, and a variety
82 of seismic slip behaviors are, in part, controlled by the interaction between *in-situ* stresses
83 (their orientations and magnitudes), the mechanical and geometrical properties of crustal
84 faults, and pore pressure (Jaeger et al., 2009; Schellart & Rawlinson, 2013; Vavrycuk, 2015).
85 Furthermore, seismic cycling and slip on faults are known to drive temporal changes in the
86 stress state on adjacent fault planes and surrounding rocks (Brodsky et al., 2017, 2020;
87 Hardebeck & Okada, 2018; K. F. Ma et al., 2005; Seeber & Armbruster, 2000; Stein, 1999).
88 For example, significant principal stress rotations followed the 2011 M_w 9.0 Tohoku
89 earthquake in Japan, 2010 M_w 8.8 Maule earthquake in Chile; and 2004 M_w 9.2 earthquake in
90 Sumatra-Andaman are suggested to be related to near-complete stress drops (Hardebeck,
91 2012). Therefore, quantitative knowledge of stress is an essential step to characterize and
92 understand the nature and causes of earthquake processes, the mechanical behavior of plate
93 boundary faults, the origin and controls of diverse fault slip patterns; and to better assess
94 seismic and tsunamigenic hazards along subduction zones (Huffman & Saffer, 2016; Riedel
95 et al., 2016; Wu et al., 2019).

96 The Hikurangi Subduction Margin (HSM), New Zealand displays along-strike variation in
97 plate interface slip behavior, ranging from episodic SSEs and creep at the northern and

98 central HSM, to deep interseismic locking beneath the southern North Island (Wallace &
99 Beavan, 2010) (Figure 1a). Creep and shallow (<15 km depth) SSEs, lasting for 2–3 weeks,
100 recur every 1 to 2 years offshore the northern and central HSM (Wallace, Beavan, et al.,
101 2012) (Figure 1a). Deep (>25 km), long-term (>1 year) SSEs occur approximately every ~5
102 years at the southern HSM (Wallace & Beavan, 2010), down-dip from a portion of the plate
103 interface that is locked and accumulating stress (Wallace et al., 2009). The physical processes
104 controlling SSEs are currently debated, with studies suggesting they are linked to the
105 frictional properties of fault zone materials (e.g., strength and coefficient of friction), low
106 effective stress linked to high pore pressure, fault heterogeneity, and fault rheology (Ando et
107 al., 2012; Kodaira et al., 2004; Kurzwski et al., 2018; Saffer & Wallace, 2015). More than
108 80% of HSM historic earthquakes and $M_w \geq 6$ earthquakes occur on upper plate (≤ 30 km)
109 faults or at the plate interface (Figure 1a) (Doser & Webb, 2003; Downes, 2006; Grapes &
110 Downes, 1997; Webb & Anderson, 1998). Earthquakes located within the subducting slab or
111 at the plate interface have also been known to trigger slope failures or series of smaller
112 earthquakes hosted on upper plate faults, some of which can be tsunamigenic (Beetham et al.,
113 2018; Lange & Moon, 2004; Power et al., 2008).



114
 115 **Figure 1.** (a) Map of the tectonic structures and regions that have experienced cumulative slow slip of
 116 ≥50 mm between 2002 and 2012 in North Island, New Zealand (Wallace & Eberhart-Phillips, 2013).
 117 Fault traces from Barnes et al. (2010), Langridge et al. (2016), Mountjoy and Barnes (2011), and
 118 Pedley et al. (Pedley et al., 2010). Yellow stars are historic earthquakes (Doser & Webb, 2003;
 119 Downes, 2006; Grapes & Downes, 1997; Webb & Anderson, 1998) and $M_w \geq 6$ earthquakes from
 120 August 2000 to 2022 (<https://www.geonet.org.nz/>). Black arrows indicate long-term relative motion
 121 between Pacific and Australian plates (Beavan et al., 2002). Blue arrows show motion of the Pacific
 122 Plate relative to overriding plate (or normal component of Pacific-Australian plate motion). (b) Map
 123 showing borehole-derived S_{Hmax} orientations (Behboudi et al., 2022; Mcnamara et al., 2021), and focal
 124 mechanisms derived S_{Hmax} orientations (Townend et al., 2012). Abbreviations: NIDFB = North Island
 125 Dextral Fault Belt; TVZ = Taupo Volcanic Zone.

126 Shallow horizontal stress orientations within the HSM have recently been constrained via
 127 borehole data analyses (Behboudi et al., 2022; Griffin, 2019; Griffin et al., 2021; Heidbach et

128 al., 2018; Lawrence, 2018; McNamara et al., 2021). Behboudi et al. (2022) provides a
129 comprehensive overview of the along-strike and depth related variability in HSM stress
130 orientations. Borehole-derived S_{Hmax} orientations rotate from ENE-WSW ($065^{\circ}/245^{\circ} \pm 10^{\circ}$)
131 in the central HSM to WNW- ESE ($112^{\circ}/292^{\circ} \pm 20^{\circ}$) and NW- SE ($140^{\circ}/320^{\circ} \pm 22^{\circ}$) in the
132 southern HSM (Figure 1b). Deep stress orientations are defined by focal mechanism
133 inversions (Townend et al., 2012), shear wave anisotropy (Illsley-Kemp et al., 2019), and
134 gravitational stresses (Evanzia et al., 2017). Earthquake focal mechanism solutions (≤ 60 km
135 depth) indicate a regional S_{Hmax} orientation of $060^{\circ}/240^{\circ} \pm 17^{\circ}$ and $066^{\circ}/246^{\circ} \pm 22^{\circ}$ in the
136 central and southern HSM, respectively (Figure 1b) (Behboudi et al., 2022; Townend et al.,
137 2012).

138 The characterization of stress magnitudes at the HSM are currently limited to relative stress
139 magnitudes derived from earthquake focal mechanisms at seismogenic depths (Townend et
140 al., 2012), and direct measurements of the minimum principal stress magnitudes (σ_3), vertical
141 stress magnitudes (S_v), pore pressures (P_p) at shallow depths (< 3 km) (Burgreen-Chan et al.,
142 2016; D. Darby & Ellis, 2001; D. Darby & Funnell, 2001), and stress regime in one borehole
143 (Tuhara-1A) in the central HSM (HRT, 2000). Observations of relative stress magnitudes
144 (≤ 60 km) by Townend et al. (2012) indicate a predominantly strike-slip and normal faulting
145 regime along the HSM. P_p measured from repeat formation tests (RFTs) and modular
146 dynamic tests (MDTs), and inferred from drilling mud weights reveal shallow (< 3 km)
147 overpressures within the upper plate of the central HSM (Burgreen-Chan et al., 2016; D.
148 Darby & Funnell, 2001). High pore pressure in central and northern HSM are attributed to
149 disequilibrium compaction of Miocene sediments and porosity reduction due to high
150 horizontal compressive stresses associated with subduction of Hikurangi Plateau beneath the
151 continental crust of North Island, New Zealand (Burgreen-Chan et al., 2016; David Darby &
152 Funnell, 2001). σ_3 magnitudes determined from leak-off tests are less than or close to S_v
153 magnitudes (Burgreen-Chan et al., 2016), suggesting variable normal, strike-slip, and a
154 reverse faulting regimes along the HSM.

155 In this study, we apply an indirect approach to constrain the three principal stress magnitudes
156 along the shallow HSM crust using openly available borehole data. We discuss our findings
157 in the context of understanding the upper plate tectonics within the HSM forearc. This study,
158 in combination with stress orientation studies already completed for the HSM, provides a
159 deeper insight into the variable tectonic behaviors associated with subduction margins, and
160 will serve as crucial information to assist in future hazard assessments of this region.

2 Geologic setting and background

The HSM at the east coast of North Island, New Zealand is a site of recent significant scientific investigation into the complexity of subduction dynamics. The HSM is formed by westward subduction of the oceanic crust of the Hikurangi Plateau beneath the continental crust of the North Island of New Zealand (Davy, 1992; Davy et al., 2008). The oblique relative motion of the Australian-Pacific plate increases from ~ 31 mm/year in the southern to ~ 48 mm/year in the northern North Island (Figure 1a) (Wallace et al., 2004). Tectonic deformation across the HSM ranges from subduction-related shortening at the Hikurangi Trough, strike-slip faulting along the North Island Dextral Fault Belt (NIDFB), and back-arc extensional tectonics in the Taupo Volcanic Zone (TVZ) at the center of North Island (Wallace et al., 2004; Figure 1a). The East Coast forearc has rotated at rate of 3° – 4° /Myr relative to the Australian plate, resulting in the TVZ back-arc rifting, strike-slip and/or normal faulting in the onshore portion of the northern and central HSM, transpressional faulting in the southern HSM, and a large along-strike variation in convergence rate at the Hikurangi Trough (Figure 1a) (Fagereng & Ellis, 2009; Nicol et al., 2007; Wallace et al., 2004; Wallace, Fagereng, et al., 2012). The oblique motion of the Australian-Pacific plate is partitioned into a margin-perpendicular component and a margin-parallel component. The margin-perpendicular component occurs along the Hikurangi subduction interface and provides NW-SE shortening mostly accommodated by slip on the subduction interface ($>80\%$) and active frontal thrusts in the overriding plate (Nicol & Beavan, 2003). The margin-parallel component is largely accommodated by a combination of right-lateral strike-slip on the North Island Dextral Fault Belt (NIDFB) and clockwise rotation of the North Island forearc (Beanland & Haines, 1998; Nicol et al., 2007; Wallace et al., 2004).

3 Methodology and Data

3.1 Data Sources and Limits

Data used in this study is sourced from 44 boreholes along the HSM (Figure 1), 41 of them are located within the onshore forearc and 3 are located offshore the east coast of NZ but west of the Hikurangi Trough. Data utilised includes wireline logging acquired over the period 1967-2013 from 0 to a maximum depth of 4350 m below ground level. Wireline data includes density logs from 26 boreholes, sonic velocity logs from 24 boreholes, and borehole image logs from 10 boreholes. Data presented here include the analysis of 21 leak-off tests and 39 formation integrity tests from 30 boreholes spanning a depth range of 3 71.5 to 3610.6

193 m, mud weight logs from 44 boreholes, and repeat formation test results from 2 boreholes
194 spanning a depth range of 1335-2700 m. How each of these data are utilised in determining
195 aspects of the in situ-stress magnitudes across the HSM is detailed below. All depths in this
196 study is referenced to ground level for onshore boreholes and sea level for offshore
197 boreholes.

198 **3.2 Vertical stress magnitude (S_v)**

199 Assuming the vertical stress (S_v) is aligned to one of the principal stresses, the S_v magnitude
200 at any specific subsurface depth can be determined by the integration of rock densities from
201 the surface to the depth of interest (equation 1):

$$S_v = \rho_w g Z_w + \int_{Z_w}^Z \rho(Z) g dZ \approx \rho_w g Z_w + \bar{\rho} g (Z - Z_w) \quad 1$$

202 where ρ_w is the average seawater density (1.03 g/cm³), g is the gravitational acceleration
203 constant (~ 9.81 m/s²), Z_w is the depth of the water column (m), Z is the depth of interest
204 (m), $\rho(Z)$ (g/cm³) is bulk density of the rock as a function of depth, and $\bar{\rho}$ (g/cm³) is the
205 average density of the rock column above Z . For onshore boreholes, Z_w is equal to zero.

206 We utilise 26 density wireline logs to estimate S_v profiles. At times wireline density logs are
207 not acquired within the top depth intervals of drilled boreholes, the rock density is
208 extrapolated from the top of a density log to the surface (seafloor for offshore boreholes) to
209 more accurately determine a complete S_v profile. This study uses several extrapolation
210 methods: 1) using wireline sonic logs to convert compressional velocity to density values in
211 boreholes where checkshot data or vertical seismic profile (VSP) surveys are available
212 (Kereru-1, Hawke Bay-1, Opoutama-1, Whakatu-1, Ngapaeruru-1, Tawatawa-1, and
213 Titihaoa-1), 2) using average densities from nearby boreholes with similar stratigraphy (e.g.
214 boreholes Kauhauroa-1, Kauhauroa-2, Kauhauroa-5, Makareao-1, and Tuhara-1A are all
215 within <20 km of each other), or 3) using standard Gardner's relationship (Gardner et al.,
216 1974) and/or regional Gardner's relationship (Table S5 in in Supporting Information S1) to
217 convert compressional velocity data from sonic wireline logs to density data logs (e.g. Hawke
218 Bay-1, Rere-1). All density logs used in this study, supplied by the New Zealand Petroleum
219 and Minerals group (NZPM), have been undergone borehole environmental corrections.

220 **3.3 Minimum principal stress magnitude (σ_3)**

221 σ_3 can be measured directly from pressure-time plots produced during leak-off tests (LOTs),
222 extended leak-off tests (XLOTs), or mini-frac tests (Addis et al., 1998; Bell, 2003; White et

223 al., 2002; Zoback et al., 2003). In the HSM, LOTs are the most common tests available to
224 calculate *in-situ* σ_3 magnitudes. LOTs are pumping pressure tests conducted in a borehole a
225 few meters below recently set casing shoes. During constant fluid volume pumping, the
226 recorded fluid pressure increase stops behaving linearly with time as the injected fluid
227 pressure surpasses the σ_3 confining stress around the borehole and fluid starts to penetrate
228 into the formation around the borehole (Addis et al., 1998; Bell, 1996). The point when the
229 fluid pressure-time curve becomes non-linear (leak-off pressure (LOP)) can be read as an
230 approximation of σ_3 magnitude. If a LOT is stopped at any point before the LOP is reached
231 the test is called a formation integrity test (FIT) and fluid pressure has not exceeded σ_3
232 magnitude. In this case, the final fluid pressure value recorded during the FIT can be used as
233 an estimate of the lower boundary of the σ_3 magnitude (e.g. Makareao-1, Zoback et al.,
234 2003).

235 In the majority of boreholes studied here the validity and accuracy of LOTs cannot be
236 assessed as the pressure–time record data is not fully reported, with only the final LOP being
237 provided in the text reports by drilling companies. Furthermore, pressure–time records are
238 sometimes estimated by only a few distinct data points, obtained from pressure measurements
239 on fluctuating gauges or flow rate estimations from counting pump strokes, making it
240 impossible to determine the specific and accurate LOP values (Zoback, 2007). It is therefore
241 possible for σ_3 to be reported slightly higher or extremely close to S_v when the measurements
242 are not carefully taken or reported. Further consideration for subduction margins is provided
243 by Couzens-Schultz and Chan (2010), who demonstrate that in active compressional settings
244 and seismically active regions, LOTs cause shear failure along pre-existing fractures rather
245 than generating new tensile fractures, leading to an underestimation of the σ_3 magnitude.

246 We first calculate $\sigma_3:S_v$ for all boreholes for which LOP measurements are available and then
247 use the average of these data to extrapolate the σ_3 values beyond the depth of measurements.
248 The FIT: S_v and $\sigma_3:S_v = 1$ are used to define the lower and upper limit of the σ_3 profile,
249 respectively.

250 **3.4 Maximum horizontal stress magnitude (S_{Hmax})**

251 **3.3.1 S_{Hmax} estimation from borehole failure analysis**

252 When a vertical borehole is drilled into a homogeneous, isotropic, and elastic medium
253 parallel to one of the three principal stress orientations, the stress at the borehole wall is

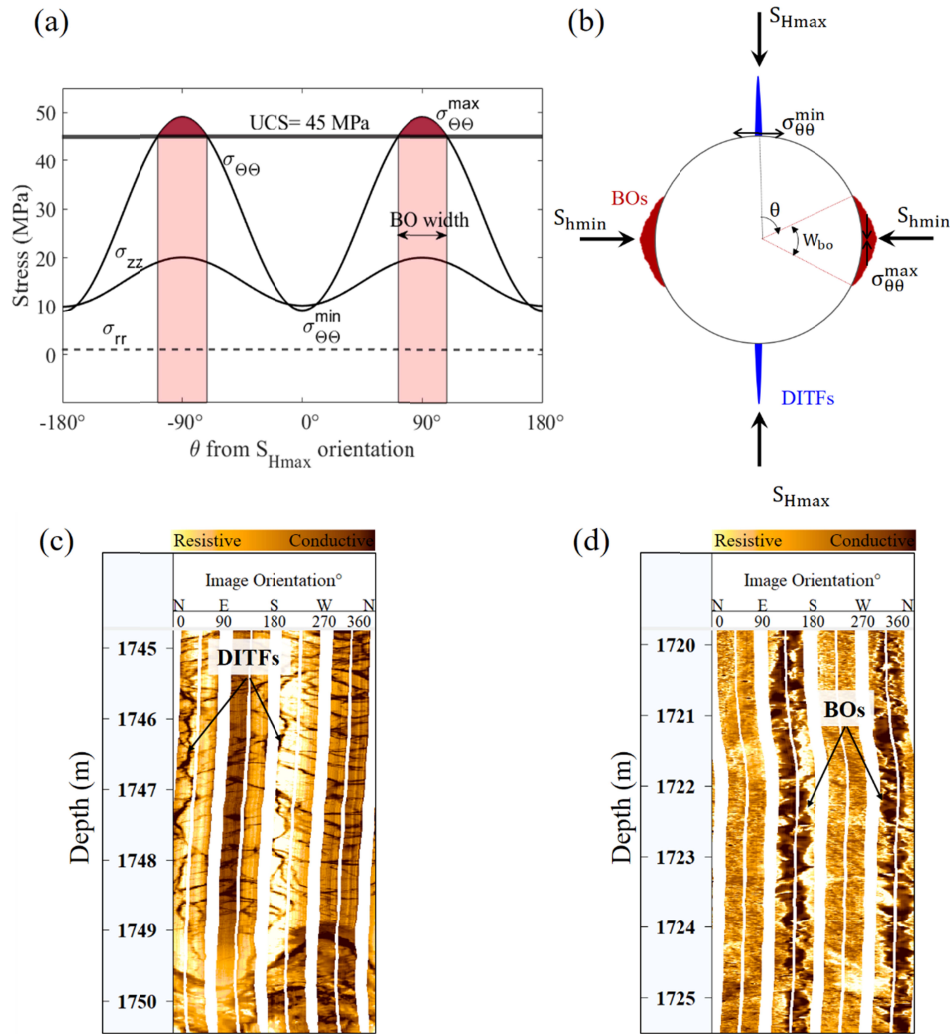
254 redistributed regarding to non-uniform, far-field principal stresses (Jaeger et al., 2009;
 255 Zoback, 2007). Assuming far field principal stresses are vertical and horizontal, the local
 256 principal effective stresses at a vertical borehole wall can be defined (Moos & Zoback, 1990;
 257 Zoback, 2007):

$$\sigma_{\theta\theta} = S_{H_{\max}} + S_{h_{\min}} - 2\cos 2\theta (S_{H_{\max}} - S_{h_{\min}}) - P_p - \text{APRS} \quad 2a$$

$$\sigma_{ZZ} = S_v - 2\vartheta \cos 2\theta (S_{H_{\max}} - S_{h_{\min}}) - P_p \quad 2b$$

$$\sigma_{rr} = \text{APRS} - P_p \quad 2c$$

258 where $\sigma_{\theta\theta}$ is the effective hoop stress (acting parallel to the borehole wall), σ_{ZZ} is the
 259 effective vertical stress, σ_{rr} is the effective radial stress (acting perpendicular to the borehole
 260 wall), $S_{H_{\max}}$ and $S_{h_{\min}}$ are the maximum and minimum horizontal principal stress magnitudes,
 261 ϑ is Poisson's ratio, APRS is the annulus pressure at the time of borehole failure (or mud
 262 weight pressure), P_p is pore pressure, and θ is the angle between the edge of borehole
 263 breakout and the $S_{H_{\max}}$ orientation (Figure 2a & 2b).



264
 265 **Figure 2.** (a) Borehole schematic showing local principal stresses ($\sigma_{\theta\theta}$, σ_{zz} , and σ_{rr}) at the borehole
 266 wall as a function of azimuth (θ) measured relative to S_{Hmax} orientation and presence of breakouts for
 267 an example in which $S_{Hmax} = 50$ MPa, $S_v = 45$ MPa, $S_{Hmin} = 40$ MPa, and UCS=45 MPa. The red
 268 shaded region shows schematically the circumference where $\sigma_{\theta\theta}$ is large enough to exceed the
 269 compressional strength of the formation and induce BOs. (b) Diagram of a borehole cross-section
 270 showing the relationship between BOs, DITFs, and the horizontal principal stress orientations. (c)
 271 Example of DITFs as they appear on a resistivity image log. (d) Examples of BOs as they appear on a
 272 resistivity image log. Figures 2c-d are from resistivity image logs of borehole Kauhauroa-5.
 273 Abbreviations: UCS = unconfined compressive strength; BO = borehole breakout; DITF: drilling
 274 induced tensile fracture.

275 Where local effective stresses exceed the tensile or compressive rock strength of the
 276 formation around the borehole, borehole failures such as drilling induced tensile fractures
 277 (DITFs) and borehole breakouts (BOs) can form, respectively (Figure 2a). Measurements of
 278 the properties of these borehole failures, e.g. the azimuth angle of BOs and/or DITFs and the

279 angular width of BOs can be used to determine *in-situ* principal stress orientations and to
 280 calculate in situ stress magnitudes present at the time of drilling.

281 DITFs form on the borehole wall where local effective stress concentrations around the
 282 borehole wall lead to a minimum $\sigma_{\theta\theta}$ less than the tensile strength of the rock ($\sigma_{\theta\theta}^{\min} \leq 0$)
 283 (Aadnoy, 1990), at a borehole azimuth parallel to S_{Hmax} ($\theta=0^\circ/180^\circ$) (Figure 2b) (Aadnoy,
 284 1990; Bell, 2003; Bell & Gough, 1979; Brudy & Zoback, 1999). DITFs typically appear as
 285 narrow, conductive (on resistivity image logs) or low amplitude and slower travel time (on
 286 acoustic image logs) pairs, $\sim 180^\circ$ from each other around the borehole wall circumference
 287 (Figure 2c). DITFs are generally parallel or slightly inclined to the borehole axis in vertical to
 288 semi-vertical boreholes (Brudy & Zoback, 1999; Zoback, 2007). Where DITFs are observed
 289 the magnitude of the far-field S_{Hmax} can be constrained using Equation 4 (Zoback, 2007):

$$3S_{hmin} - T_0 - P_p - APRS - \sigma^{\Delta T} \leq S_{Hmax} \quad 3$$

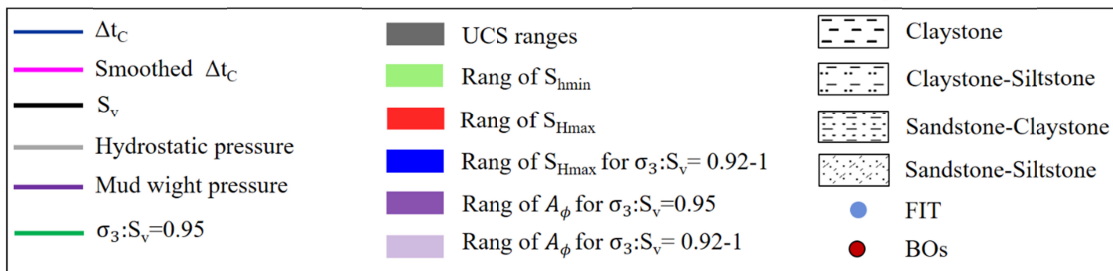
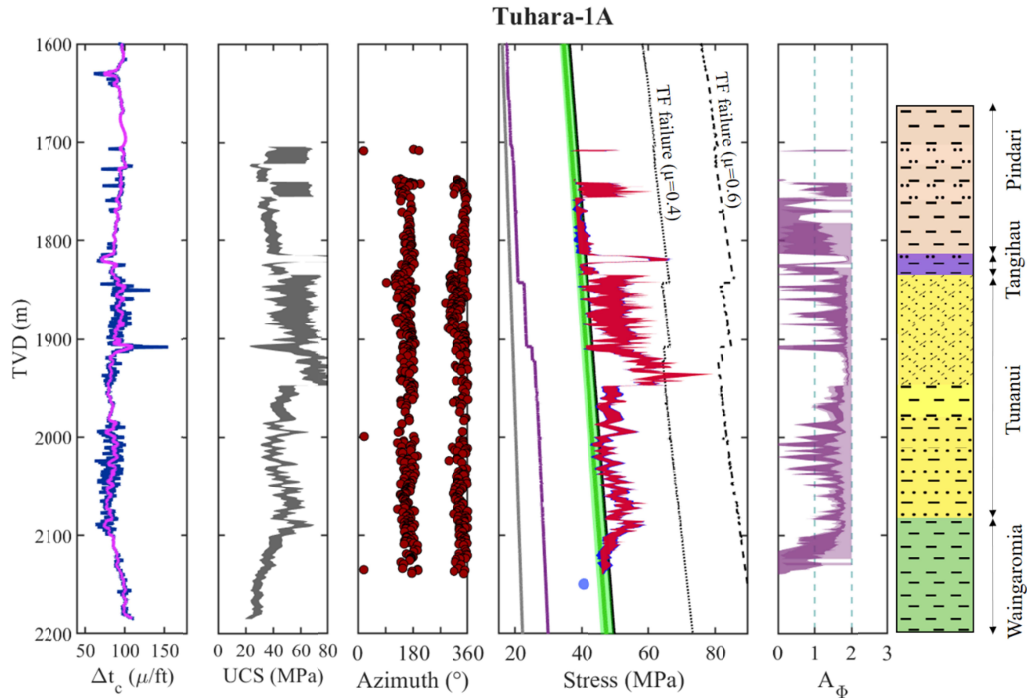
290 where S_{Hmax} and S_{hmin} are maximum and minimum horizontal principal stresses respectively,
 291 T_0 is the formation tensile strength, P_p is pore pressure, APRS is annulus pressure (or mud
 292 weight), and $\sigma^{\Delta T}$ is thermal stress arising from the difference between the drilling mud
 293 temperature and formation temperature. $\sigma^{\Delta T}$ is applied where there is a noticeable difference
 294 between mud and rock temperature, such as geothermal boreholes. The tensile rock strength
 295 in sedimentary rocks is often quite small (a few MPa) and can be assumed to be zero in the
 296 analysis of DITFs (Brudy & Zoback, 1999). In this study, $\sigma^{\Delta T}$ is considered negligible.

297 BOs form as enlargements of the borehole diameter on opposite sides of the borehole wall
 298 where $\sigma_{\theta\theta}$ is large enough to exceed the formations compressional strength (Figure 2a) (Bell
 299 & Gough, 1979; Zoback, 2007). The $\sigma_{\theta\theta}$ magnitude reaches a maximum at $\theta=\pm 90^\circ$ (Figure
 300 2a), which occurs at a borehole azimuth oriented perpendicular to the S_{Hmax} direction (Figure
 301 2b). BOs typically appear as a pair of wide, out-of-focus, conductive (in water-based mud;
 302 Figure 2d) or resistive (in oil-based mud) zones on resistivity image logs, or as zones of low
 303 acoustic amplitude and slower travel time on acoustic image logs. BOs are located $\sim 180^\circ$
 304 from each other around the circumference of the borehole wall (Figure 2b & 2d). S_{Hmax}
 305 magnitudes can be estimated by measuring BO widths (W_{bo}) from borehole image logs using
 306 Equation 5 (Barton et al., 1988; Vernik & Zoback, 1992):

$$S_{Hmax} = \frac{(UCS+P_p+APRS+\sigma^{\Delta T})-S_{hmin}(1+2 \cos(\pi-W_{bo}))}{1-2 \cos(\pi-W_{bo})} \quad 4$$

307 where W_{bo} is the angular width of the BO; UCS is unconfined compressive strength of the
308 formation, P_p is pore pressure, APRS is annulus pressure or mud weight, S_{hmin} is the minimum
309 horizontal principal stress magnitude, and $\sigma^{\Delta T}$ is the thermal stress effect resulting from the
310 difference between the drilling mud temperature and formation temperature. In this study,
311 $\sigma^{\Delta T}$ is considered negligible.

312 UCS is a key parameter in estimating S_{Hmax} magnitude (Equation 4), and can either be
313 directly measured from laboratory strength tests on core samples, or estimated using
314 empirical relationships between UCS and other rock properties (Chang et al., 2006). Direct
315 measurements of rock strength are rare for the HSM. Borehole Waingaromia-2 in the
316 northern HSM is the only borehole where a laboratory strength test was conducted on
317 calcareous claystone and mudstone core samples (acquired from 132 and 362 m measured
318 depth, respectively), providing UCS values of 1.1-1.2 MPa and friction angles of 20.5°-32.1°
319 (friction coefficient 0.37-0.64) (Indo-Pacific Energy (NZ) Ltd., 2002). However, no
320 relationship between P-wave slowness (Δt_c) and UCS was established because no
321 geophysical logs were obtained and velocity measurements on core samples are unavailable.
322 Therefore, in this study, UCS values are indirectly estimated by using empirical relationships
323 between rock strength and Δt_c . Empirical equations have been developed for different rock
324 types, relating various rock properties to UCS across the world. In this study we utilize a
325 variety of empirical relationships between UCS and sonic velocity by matching appropriate
326 equations to dominant lithologies encountered along each studied borehole in an effort to
327 reduce uncertainty in UCS values and thus S_{Hmax} magnitude values. Upper and lower bounds
328 of the UCS are determined using various published empirical relationships (Chang et al.,
329 2006) to provide a range of possible S_{Hmax} magnitudes (Figure 3). Details on the equations
330 used in individual boreholes to determine the lower and upper limits of UCS can be found in
331 Table S1, Table S2, and S3 in Supporting Information S1.



332
 333 **Figure 3.** Calculated far-field in situ stress magnitudes, referenced to the sea level in borehole
 334 Tuhara-1A. (a) P-wave slowness (blue line) de-spiked and smoothed over 3m intervals (pink line). (b)
 335 Range of UCS values derived from P-wave slowness using relations in Table S2 and S3 (c) Azimuth
 336 of borehole BOs. (d) Calculated S_v (solid black line), S_{hmin} (green field), and S_{Hmax} (red field)
 337 magnitudes by considering that pore pressure is equal to mud weight. The hydrostatic pressure (grey
 338 line) is computed assuming a sea water density of 1.03 g/cc. The σ_3 and the range of S_{hmin} is
 339 determined from the average $\sigma_3:S_v = 0.95$ and $\sigma_3:S_v = 0.92-1$, respectively. Abbreviations: Δt_c : P-
 340 wave slowness; UCS = uniaxial compressive strength; BO = borehole breakout; FIT = formation
 341 integrity test; TF failure: thrust faulting failure; μ : friction coefficient; S_v : vertical stress; S_{hmin} :
 342 minimum horizontal stress; S_{Hmax} : maximum horizontal stress; σ_3 : minimum principal stress; A_ϕ :
 343 Tectonic stress regime index.

344 A further important parameter required to calculate S_{Hmax} magnitudes and effective stresses is
 345 P_p . Direct P_p measurements tests such as RFTs and MDTs are the most reliable measurements
 346 (Gunter & Moore, 1986; Zoback, 2007). However, these direct P_p measurements are difficult
 347 to acquire, particularly in low permeability formations, and are often only conducted at

348 depths where possible overpressures may exist (Dutta et al., 2021; Lee et al., 2022; Y. Z. Ma
349 & Holditch, 2015; Zoback, 2007). Drilling mud weight logs can provide indirect, continuous
350 approximations of the P_p along a borehole, and can be used as a proxy of P_p assuming the
351 mud weights have been chosen to stabilize the borehole during drilling, and if no significant
352 mud losses or kicks are reported (Van Ruth et al., 2002) . Mud Losses of greater than 25
353 bbl/hr for water-based mud (Zhang & Yin, 2017) may indicate that annulus pressure
354 exceeded P_p or/and σ_3 value, resulting in the loss of fluids into the formation. While kicks
355 and high fluid influx indicate that P_p is greater than the annulus pressure. In both cases, the
356 P_p derived from drilling mud weight logs should be corrected to generate a good estimation
357 of P_p . In this study we use mud weight logs from 44 boreholes to calculate P_p . Minor
358 seepage (mud losses <22 bbl/hr) is reported for boreholes Kauhauroa-2/5, Makareao-1,
359 Tuhara-1A, Ngapaeruru-1, Tawatawa-1, and Titihaoa-1, and Ranui-2 in the intervals where
360 BOs are observed, providing confidence in the use of mud weight logs in those intervals for
361 P_p determination. A minor mud loss of 28 bbl/hr has been observed at severely fractured
362 depth interval of 1030-1225 m TVD in borehole Ngapaeruru-1 which was treated by remedial
363 techniques and procedures easily. Moreover, minor background gas and fluid influx are
364 reported in boreholes Kahauuroa-5, Makareao-1, Tuhara-1A, Tawatawa-1, and Titihaoa-1,
365 which were controlled by mud weight such that they never flowed. Since no significant mud
366 losses or kicks are reported in the depth intervals where BOs are observed, we consider the
367 annulus pressure records a good proxy of P_p in those depth intervals.

368 The P_p calculated from mud weight logs in Kauhauroa-5 and Titihaoa-1 boreholes are further
369 calibrated using direct P_p measurements obtained from RFTs. Formation tests conducted in
370 17 further HSM boreholes (Awatere-1, Hukarere-1, Kauhauroa-2/3/4B, Kiakia-1A,
371 Makareao-1, Mangaone-1, Morere-1, Opoutama-1, Ruakituri-1, Takapau-1, Te Hoe-1,
372 Tuhara-1A/1B, Waitahora-1, and Waitaria-2) are not included in this study due to incomplete
373 pressure build ups during testing in low-permeability formations, test seal failures, or tests
374 conducted in formation intervals supercharged to hydrostatic pressure.

375 **3.3.2 S_{Hmax} magnitude estimation from frictional limit theory**

376 To constrain S_{Hmax} magnitudes that result in the observed BO and DITF occurrences, the
377 stress state is assumed to be limited by Coulomb frictional sliding on an optimally oriented
378 and pre-existing fault plane (Zoback, 2007). This means that the maximum effective principal

379 stress cannot exceed the stress value required to cause slip, defined by the friction coefficient
380 (μ) of adjacent faults, on a critically oriented fault plane (Jaeger et al., 2009; Sibson, 1974):

$$\frac{(\sigma_1 - P_p)}{(\sigma_3 - P_p)} \leq ((1 + \mu^2)^{0.5} + \mu)^2 \quad 5$$

381 where σ_1 is the maximum principal stress, σ_3 minimum principal stress, P_p is pore pressure,
382 and μ is coefficient of friction on an optimally oriented, cohesionless, pre-existing fault.

383 This constraint is typically displayed as a stress polygon, which shows the permissible values
384 of horizontal principal stress magnitudes for a specific depth, S_v , μ , and P_p for normal, strike-
385 slip, and thrust faulting tectonics (Zoback, 2007). Although this method only provides the
386 upper and lower limits for the S_{Hmax} magnitude, it can yield more accurate ranges of
387 permissible S_{Hmax} magnitudes when combined with S_{Hmax} magnitude estimates from borehole
388 failure analysis (Chang et al., 2010; Huffman & Saffer, 2016).

389 **3.5 Tectonic stress regime index (A_ϕ)**

390 In order to characterize a stress regime or faulting style with stress magnitude data, we use
391 the stress regime index (A_ϕ , Equation 6a and 6b) described by Simpson (Delvaux et al.,
392 1997):

$$A_\phi = (n + 0.5) + (-1)^n (R - 0.5) \quad 6a$$

$$R = (\sigma_2 - \sigma_3) / (\sigma_1 - \sigma_3) \quad 6b$$

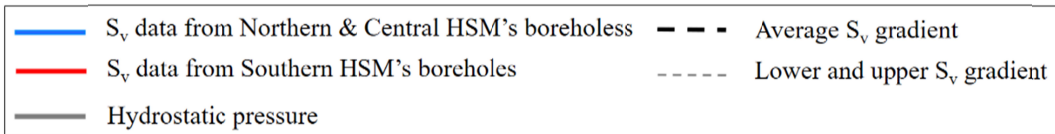
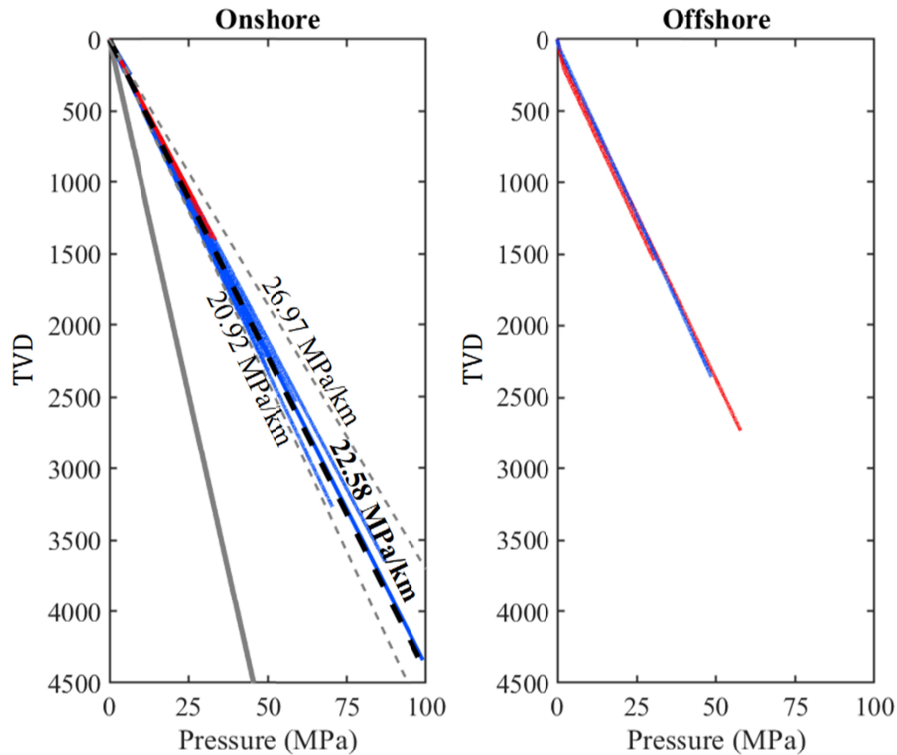
393 where n is the number of principal stress components greater than the principal stress whose
394 axis is closest to the vertical, R is the stress ratio, and σ_1 , σ_2 , σ_3 are the maximum, medium,
395 and minimum principal stress magnitudes, respectively.

396 A_ϕ values range from 0 to 1 in normal faulting regimes, 1 to 2 in strike-slip regimes, and 2 to
397 3 in thrust faulting regimes.

398 **4 Results**

399 **4.1 Vertical Stress Magnitudes**

400 S_v magnitudes determined from 24 onshore boreholes provide overburden stress gradients
401 ranging from 20.92 to 26.97 MPa/km, with a mean value of 22.58 ± 1.23 MPa/km (Figure 4a;
402 Table S5). S_v magnitudes measured within the 3 offshore boreholes range from 20.9 to 21.7
403 MPa/km with a mean value of 21.26 ± 0.4 MPa/km.



404
405 **Figure 4.** S_v gradient profiles from boreholes in the a) HSM onshore and b) HSM offshore. S_v :
406 vertical stress.

4.2 Minimum Principal Stress Magnitudes

407
408 σ_3 magnitudes calculated from LOT data range from 1.9 MPa at 102.3 m TVD (borehole
409 Waitaria-2) to 77.9 MPa at 3610.6 m TVD (borehole Rere-1) (Table 1). For all examined
410 LOT data (with the exception of one test in borehole Titihoa-1 where σ_3 derived from LOP is
411 greater than S_v), the normalized effective σ_3 ratio ranges from 0.23 to 1 (Table 1).

412

413 Table 1. σ_3 magnitudes calculated from LOP measurements.

	Borehole	Depth ^a (m)	σ_3^b (MPa)	S_v^c (MPa)	σ_3/S_v
Central HSM	Awatere-1	301.9	6.1	6.5	0.94
		1085.3	22.4	24.0	0.93
	Hawke Bay-1	386.6	7.2	7.4	0.97
		1359.6	26.4	27.7	0.95
	Kauhauroa-1	455.8	7.9	9.5	0.83
	Kauhauroa-2	463.8	8.2	10.1	0.81
	Kauhauroa-5	459.2	7.4	10.2	0.73
	Kereru-1	481.1	9.4	10.2	0.92
Kiakia-1/1A	318.6	5.7	6.9	0.83	

	Opoho-1	521.3	9.3	11.7	0.79
	Rere-1	3610.6	77.9	82.3	0.95
	Tuhara-1/1A	590.8	8.4	13.3	0.63
	Waitaria-2	102.3	1.9	2.4	0.79
Southern HSM	Ranui-1	357.3	5.2	8.6	0.6
	Tawatawa-1	722.5	12.7	12.7	1
	Titihaoa-1	614.9	9.5	11	0.86
		1585.7	30.6	32.4	0.94
		1979.8	43.4*	41.3	1.05

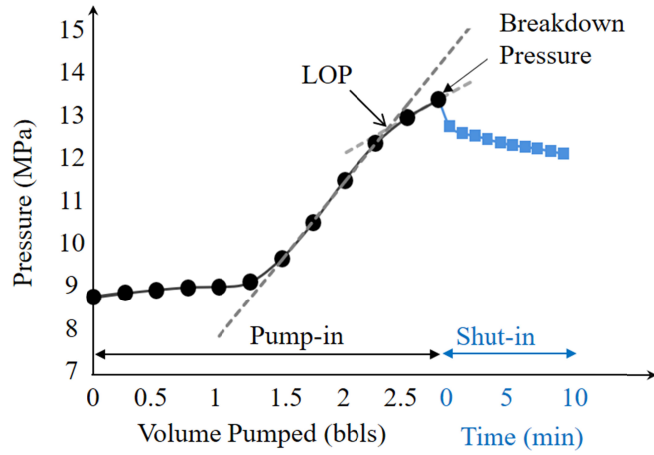
414 ^a True vertical depth from ground level for onshore boreholes and sea level for offshore
415 boreholes

416 ^b σ_3 derived from Leak-off pressure

417 ^c S_v vertical stress

418 * σ_3 derived from LOP is greater than S_v

419 LOP values measured in boreholes Tuhara-1/1A and Ranui-1 (11 m west of Ranui-2) are
420 remarkably low, such that LOP values are less than the σ_3 values estimated by normal
421 faulting failure with friction coefficients less than 0.6. In borehole Titihaoa-1, the σ_3 value
422 (43.4 MPa) derived from an LOT performed at \sim 1979.8 m TVD is greater than the S_v for this
423 depth (41.3 MPa). In this case, σ_3 is considered to be vertical, indicating a thrust/reverse
424 faulting regime (Zoback, 2007). In borehole Tawatawa-1 two LOTs were performed at 722.5
425 m TVD. The initial test yielded a LOP of 13.23 MPa, while the second LOT yielded a LOP
426 of 13.36 MPa (Tap Oil Limited, 2004). Our reassessment of pressure-time curve of the
427 second LOT (which had more data defining the time-pressure plot) reveals that the formation
428 breakdown pressure (FBP) was reported rather than LOP, resulting in an overestimation of σ_3
429 making it appear greater than the S_v for this depth. We determine the LOP of the second test
430 by intersecting the straight line of the linear section with the tangent line of the ascending
431 section on the pressure-volume curve (Figure 5), and report a σ_3 magnitude of 12.7 MPa,
432 almost equal to S_v (13 MPa). Assuming σ_3 measurements made from the reported LOT data
433 in the study boreholes are a proxy of σ_3 (after correcting σ_3 derived from LOP $>S_v$ to $\sigma_3=S_v$),
434 a HSM average minimum normalized effective stress ratio of 0.66 ± 0.2 and 0.7 ± 0.3 are
435 derived for the central and southern HSM respectively (Figure 6).



436

437 **Figure 5.** Results of the leak-off test run at 722.5 m TVD in borehole Tawatawa-1. Pressure versus
 438 volume of mud pumped to the formation curve reveals that the leak-off pressure (LOP) is 12.7 MPa.

439 FIT data show the lower limit of σ_3 magnitudes are typically below S_v in most of boreholes in
 440 this study. However, in some boreholes (Table 2), FIT results are approximately equal to or
 441 greater than S_v . The entire FIT dataset for all boreholes in this region can be found in Table
 442 S3 in Supporting Information S1, and are used to constrain σ_3 profiles within boreholes where
 443 LOP measurements are not available.

444

445 Table 2. The lower limit of σ_3 values calculated from FIT data.

	Borehole	Depth ^a (m)	The lower limit of σ_3 ^b from FIT ^c (MPa)	S_v ^d (MPa)
	Central HSM	Hukarere-1	89.9	1.81
430.2			8.64	8.55
Kauhauroa-3		332.7	7.33	7.42
		999.2	22.44	22.56
Kauhauroa-4		346.1	7.63	7.36
Kauhauroa-4B		91	1.95	1.97
		538.3	11.56	11.75
Makareao-1		306.2	6.76	6.55
		484.8	10.6	10.59
Rere-1		115	2.39	2.65
		2109.4	49.56	48.17
Waitahora-1		95.8	2	2.01
	722	16.24	15.53	
	994.5	22.93	21.76	
Waitaria-2	556.1	12.53	12.85	

446 ^a True vertical depth from ground level for onshore boreholes and sea level for offshore
 447 boreholes

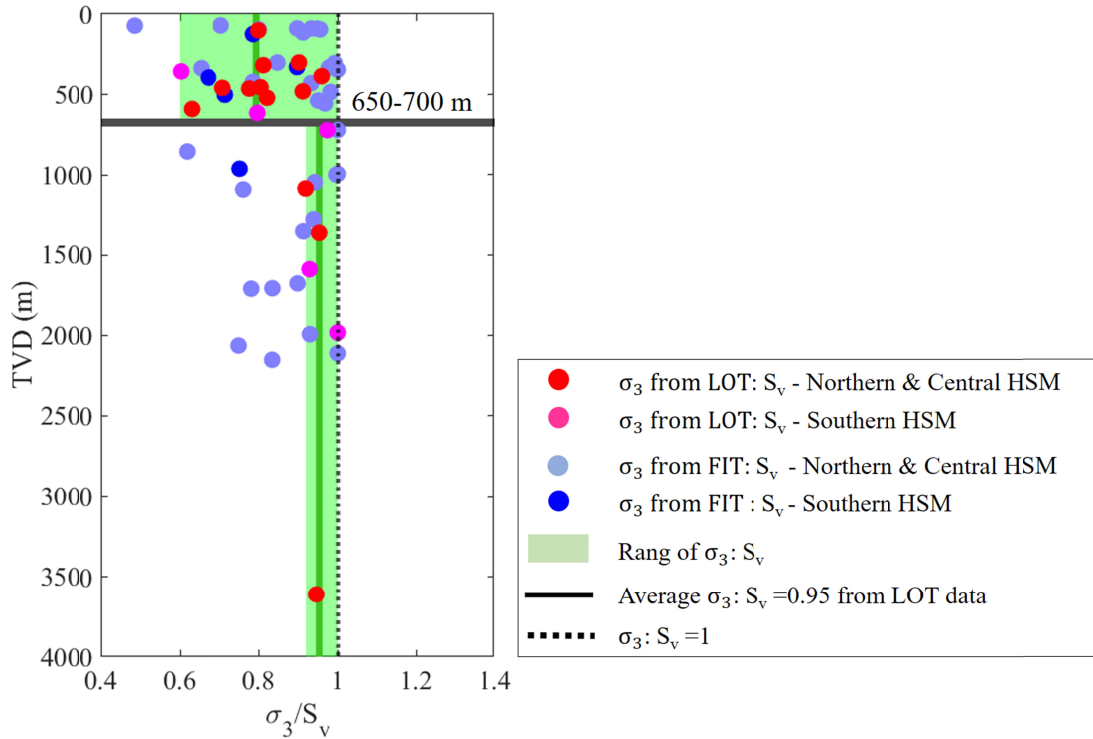
448 ^b Minimum principal stress magnitudes

449 ^c Formation integrity test

450 ^d S_v vertical stress

451

452 We calculated $\sigma_3:S_v$ (after correcting σ_3 derived from LOP and FIT $>S_v$ to $\sigma_3=S_v$) for all 21
 453 LOTs and 39 FIT measurements in the study area and found that $\sigma_3:S_v$ varies significantly
 454 above and below 650-700 m TVD (Figure 6). The $\sigma_3:S_v$ ranges from 0.6-1 at depths above
 455 650-700 m TVD, while it ranges from 0.92-1 below this depth interval (Figure 6). Above and
 456 below 650-700 m TVD, the average $\sigma_3:S_v$ values derived from LOT measurements are 0.79
 457 and 0.95, respectively.



458
 459 **Figure 6.** $\sigma_3: S_v$ along the HSM. Abbreviations: LOT: leak of test; FIT = formation integrity test; S_v :
 460 vertical stress; σ_3 : minimum principal stress.

461 In this study, to create the σ_3 profile in boreholes where LOT measurements are not available
 462 at the depth of interest, we only consider LOT and FIT measurements recorded at depths
 463 below 650-700 m TVD for two main reasons: 1) to exclude the influence of topographic
 464 effects and shallow processes such as gravitational collapse, erosion, and subsidence in the σ_3
 465 calculation, and 2) because our borehole breakouts data to estimate S_{Hmax} magnitudes in 7 out
 466 of 8 boreholes are located below 700m TVD.

467 4.3 Stress magnitude from borehole data

468 4.3.1 Central HSM (Hawke's Bay region)

469 A range of potential S_{Hmax} magnitudes are estimated along individual boreholes at depths
 470 intervals where BO widths and DITFs are measured from image logs. Further the lower and

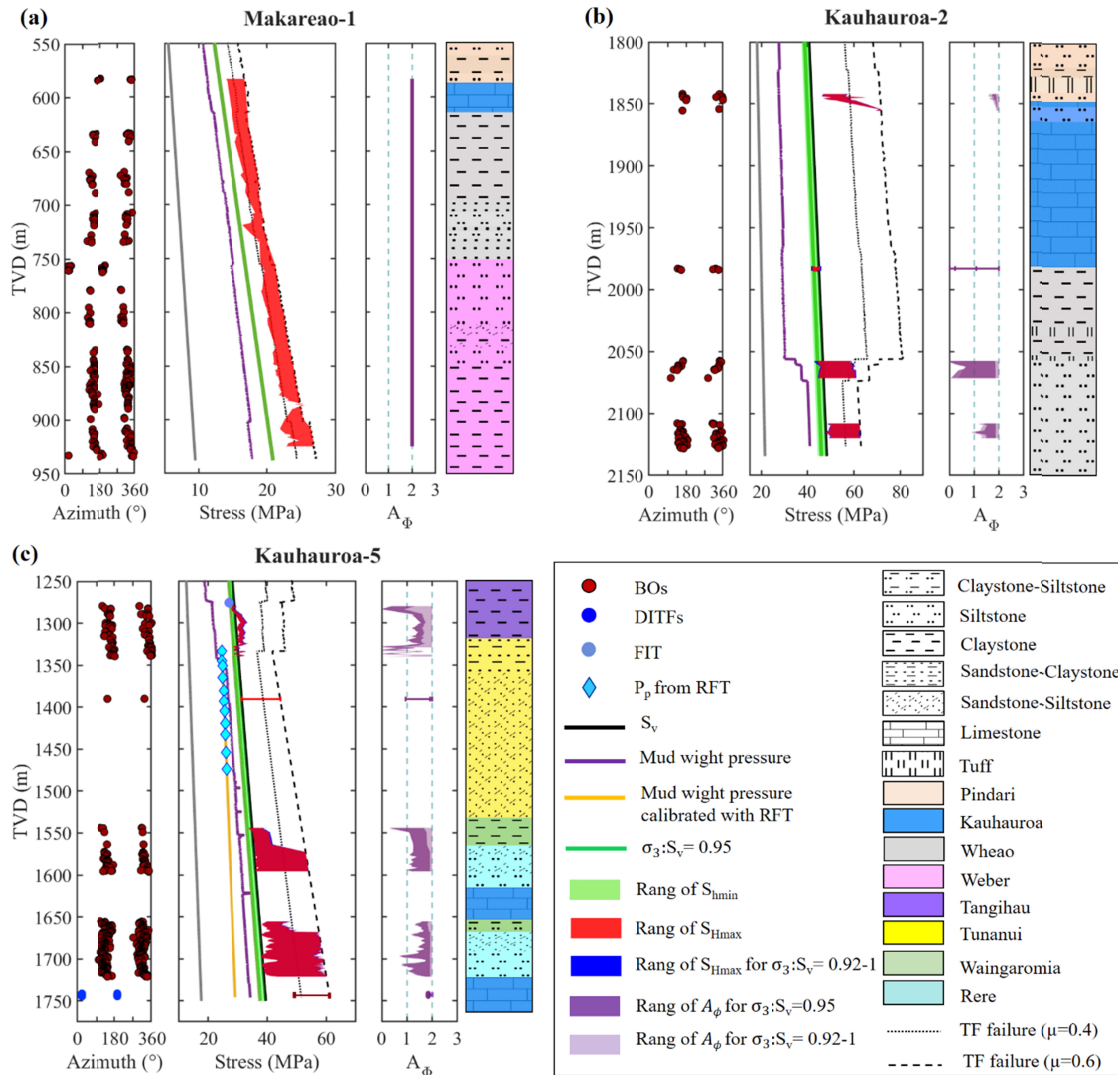
471 upper limit of S_{Hmax} magnitudes are constrained by theoretical limits provided by slip on pre-
 472 existing faults with a friction coefficient of 0.6 (described in 3.3.2).

473 **Makareao-1 borehole**

474 The $\sigma_3 : S_v$ ratios of 1.03 and 1 are determined from σ_3 values calculated using FIT data at
 475 depths 306.2 and 484.8 m TVD respectively (Table 2). The $\sigma_3 : S_v \geq 1$ indicates that $\sigma_3 = S_v$ in
 476 this borehole. The $S_{Hmax} : S_v$ ratio of 1.03-1.31 is determined for borehole Makareao-1 using
 477 the S_{Hmax} values calculated from the lower and upper value of UCS.

478 The $S_{Hmax} : S_v$ ratio of 1.03-1.31 and a $\sigma_3 : S_v = 1$ along this borehole indicates a stress regime
 479 such that $\sigma_3 = S_v < S_{Hmax}$ (Figure 7a). $A_\phi = 2$ is determined from calculated stress magnitude
 480 data in this borehole.

481



482

483 **Figure 7.** Calculated far-field in situ stress magnitudes, referenced to the sea level in borehole (a)
484 Makareao-1 (b) Kauhauroa-2 (c) Kauhauroa-5 in the central HSM. Abbreviations: Δ_{TC} : P-wave
485 slowness; UCS = uniaxial compressive strength; BO = breakout; DITF: drilling induced fracture; FIT
486 = formation integrity test; TF failure: thrust faulting failure; μ : friction coefficient; RFT: repeat
487 formation test; S_v : vertical stress; S_{hmin} : minimum horizontal stress; S_{Hmax} : maximum horizontal stress;
488 σ_3 : minimum principal stress; A_ϕ : tectonic stress regime index.

489 **Kauhauroa-2 borehole**

490 A $\sigma_3 : S_v$ ratio of 0.81 is determined from σ_3 value calculated using LOT data at 463.8 m TVD
491 (Table 1). The σ_3 values in the deeper part of the borehole are calculated from the average σ_3
492 $: S_v$ ratio of 0.95 along the HSM and are further constrained by the lower limit of σ_3 value
493 determined from an FIT= 30.23 MPa at 1707.3 m TVD. The $S_{Hmax} : S_v$ ratio of 0.95-1.71 is
494 determined for borehole Kauhauroa-2 using the S_{Hmax} values calculated from the lower and
495 upper value of UCS.

496 The $S_{Hmax} : S_v$ ratio of 0.95-1.71 and the $\sigma_3 : S_v$ ratio of 0.95 indicate a dominant stress regime
497 such that $S_{hmin} \leq S_v \leq S_{Hmax}$ (Figure 7b). A $0 \leq A_\phi \leq 1.94$ is determined from calculated stress
498 magnitude data in this borehole. S_v , S_{hmin} , and the lower limit of S_{Hmax} are nearly equal below
499 1980 m TVD such that $S_{hmin} \approx S_{Hmax} \approx S_v$.

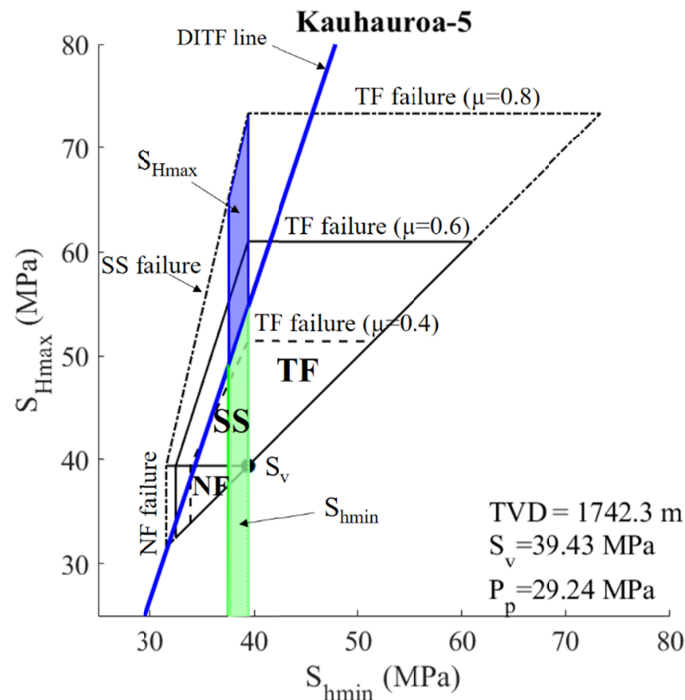
500 **Kauhauroa-5 borehole**

501 A $\sigma_3 : S_v$ ratio of 0.73 is determined from σ_3 value calculated using LOT data at 459.2 m TVD
502 (Table 1). The σ_3 values in the deeper part of the borehole are calculated from the average σ_3
503 $: S_v$ ratio of 0.95 along the HSM and are further constrained by the lower limit of σ_3 value
504 calculated from an FIT value of 27.13 MPa at 1276.1 m TVD. The $S_{Hmax} : S_v$ ratios of 0.95-
505 1.13 in 1280-1350 m TVD and 0.97-1.54 in 1390-1750 m TVD are determined in this
506 borehole using the S_{Hmax} values calculated from the lower and upper value of UCS.

507 The analysis of S_{Hmax} magnitudes and the $\sigma_3 : S_v$ ratio of 0.95 indicate a dominant $S_{hmin} \approx S_v \approx$
508 S_{Hmax} ($S_{Hmax} - S_{hmin} < 5$ MPa) and $0 \leq A_\phi \leq 1.13$ in the depth interval of 1280-1350 m TVD
509 (Figure 7c). Moving along the depth to 1390-1750 m TVD, $S_{hmin} \leq S_v \leq S_{Hmax}$ and $0.44 \leq A_\phi$
510 ≤ 1.92 are observed.

511 Further constraints on stress magnitudes are made in this borehole using the presence of
512 DITFs between 1741-1745 m on FMI borehole image logs (Figure 7c). The presence of
513 DITFs at 1742.3 m suggests that the S_{Hmax} should be above the DITF line (Figure 8), where
514 the local hoop stress can be tensile (Equation 3), but also inside the stress polygon with $\mu =$

515 0.6. The possible range of S_{Hmax} and S_{hmin} constrained using this information lie inside the
 516 blue shaded area (Figure 8) and suggest a stress state such that $S_{hmin} \leq S_v < S_{Hmax}$.
 517



518 **Figure 8.** Analysis of stress magnitudes using stress polygon defined by Coulomb friction law with a
 519 friction coefficient (μ) of 0.4 and 0.6, and 0.8 in borehole Kauhauroa-5 at depth of 1742.3 m where
 520 DITFs are observed. The green shaded area represents σ_3 range estimated from the average $\sigma_3 : S_v$ ratio
 521 of 0.95 along the HSM. The blue shaded area represents S_{Hmax} range which local hoop stress is tensile
 522 and DITFs are formed. NF: normal faulting, SS: strike-slip faulting, TF: thrust faulting; DITF: drilling
 523 induced tensile fracture.
 524

525 Tuhara-1A borehole

526 A $\sigma_3 : S_v$ ratio of 0.63 is determined from σ_3 value calculated using LOT data at 590.8 m TVD
 527 (Table 1). The σ_3 values in the deeper part of the borehole are calculated from the average σ_3
 528 $: S_v$ ratio of 0.95 along the HSM, and are further constrained by the lower limit of σ_3 value
 529 determined from FIT value of 40.6 MPa at 2149.5 m TVD. The $S_{Hmax} : S_v$ ratio of 0.95-1.81 is
 530 determined for borehole Tuhara-1A using the S_{Hmax} values calculated from the lower and
 531 upper value of UCS.

532 The $S_{Hmax} : S_v$ ratio of 0.95-1.81 and the $\sigma_3 : S_v$ ratio of 0.95 indicate a dominant stress
 533 regime such that $S_{hmin} \leq S_v \leq S_{Hmax}$ (Figure 3). A $0 \leq A_\phi \leq 1.95$ is determined from calculated
 534 stress magnitude data in this borehole.

535

4.2.2 Southern HSM

536

Ngapaeruru-1 borehole

537

The σ_3 values in this borehole are calculated from the average $\sigma_3 : S_v$ ratio of 0.95 along the

538

HSM and are further constrained by the lower limit of σ_3 value determined from FIT values

539

of 8.35 and 16.86 MPa at 501.9 and 962.7 m TVD, respectively. The $S_{Hmax} : S_v$ ratio of 0.95-

540

1.75 is determined for borehole Ngapaeruru-1 using the S_{Hmax} values calculated from the

541

lower and upper value of UCS.

542

The $S_{Hmax} : S_v$ ratio of 0.95-1.75 and the $\sigma_3 : S_v$ ratio of 0.95 indicate a dominant stress regime

543

such that $S_{hmin} \leq S_v \leq S_{Hmax}$ (Figure 9a). A $0 \leq A_\phi \leq 1.94$ is determined from calculated stress

544

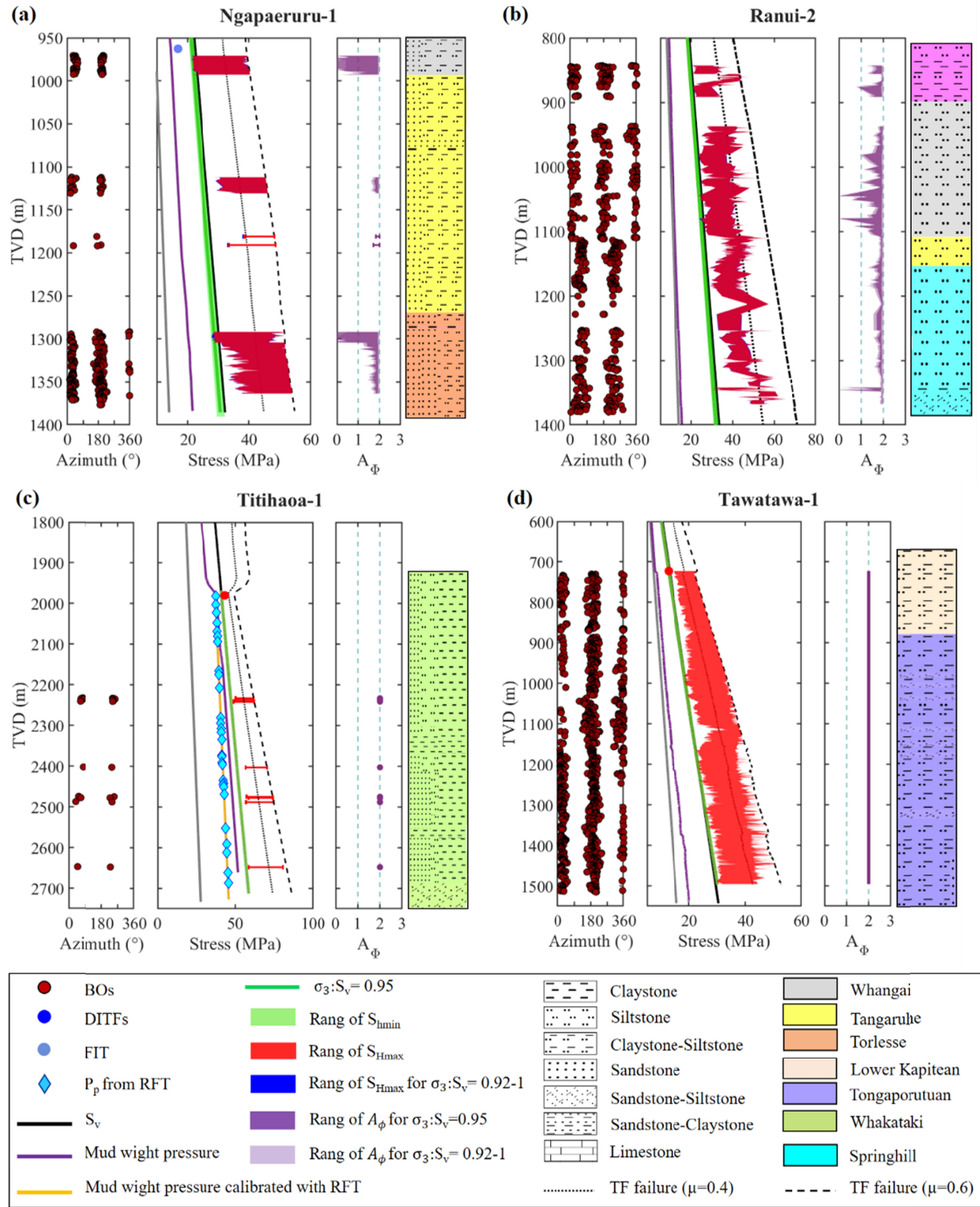
magnitude data in this borehole (Figure 9a). The upper limit of S_{Hmax} magnitudes from the

545

upper values of UCS are constrained by the limits provided by slip on pre-existing faults with

546

$\mu=0.6$.



547

548 **Figure 9.** The constrained in situ stress profile with depth in (a) Ngapaeruru-1 (b) Tawatawa-1 (c)
 549 Titihaoa-1 in the southern HSM. Abbreviations: BO = breakout; FIT = formation integrity test; LOT:
 550 leak of test; TF failure: thrust faulting failure; μ : friction coefficient; RFT: repeat formation test; S_v :
 551 vertical stress; S_{hmin} : minimum horizontal stress; S_{Hmax} : maximum horizontal stress; σ_3 : minimum
 552 principal stress; A_ϕ : tectonic stress regime index.

553

Tawatawa-1 borehole

554 A $\sigma_3 : S_v$ ratio of 1 is determined from σ_3 value calculated using LOT data at 722.5 m TVD
555 (Table 1). The $S_{Hmax} : S_v$ ratio of 1-1.82 is determined for borehole Tawatawa-1 using the
556 S_{Hmax} values calculated from the lower and upper value of UCS.

557 The $S_{Hmax} : S_v$ ratio of 1-1.82 and the $\sigma_3 : S_v = 1$ indicate a dominant stress regime such that $\sigma_3 =$
558 $S_v \leq S_{Hmax}$ (Figure 9d). The upper limit of S_{Hmax} magnitudes from the upper values of UCS
559 are constrained by the limits provided by slip on pre-existing faults with $\mu=0.6$. $A_\phi = 2$ is
560 determined from calculated stress magnitude data in this borehole.

561

Titihaoa-1 borehole

562 The $\sigma_3 : S_v$ ratios of 0.86, 0.94, and 1.05 are determined from σ_3 values calculated using LOT
563 data at 614, 1585.7, and 1979.8 m TVD in this borehole (Table 1). The $\sigma_3 : S_v$ ratio of 1.05 at
564 1979.8 m TVD indicate that $\sigma_3 = S_v$ at depth intervals of 2200-2700 m TVD. The $S_{Hmax} : S_v$
565 ratio of 1.02-1.41 are determined for borehole Titihaoa-1 using the S_{Hmax} values calculated
566 from the lower and upper value of UCS.

567 The analysis of S_{Hmax} magnitudes and $\sigma_3 : S_v = 1$ at depth intervals of 2200-2700 m TVD
568 indicate a stress regime such that $\sigma_3 = S_v \leq S_{Hmax}$ (Figure 9c). The upper limit of S_{Hmax}
569 magnitudes from the upper values of UCS are constrained by the limits provided by slip on
570 pre-existing faults with $\mu=0.6$. $A_\phi = 2$ is determined from calculated stress magnitude data in
571 this borehole.

572

Ranui-2 borehole

573 The σ_3 profile in this borehole is calculated from the average HSM $\sigma_3 : S_v$ ratio of 0.95 are
574 further constrained by the lower limit of σ_3 value determined from FIT value of 6.35 MPa at
575 395 m TVD. The $S_{Hmax} : S_v$ ratio of 0.95-3.12 are determined for borehole Ranui-2 using the
576 S_{Hmax} values calculated from the lower and upper value of UCS.

577 The $S_{Hmax} : S_v$ ratio of 0.95-3.12 and the $\sigma_3 : S_v$ ratio of 0.95 indicate a dominant stress
578 regime such that $S_{hmin} \leq S_v \leq S_{Hmax}$ (Figure 9b). A $0 \leq A_\phi \leq 1.96$ is determined from
579 calculated stress magnitude data in this borehole.

580

5 Discussion

5.1 Shallow HSM tectonics

583 Stress magnitudes calculated from borehole data indicate that the $S_{Hmax} : S_v$ ratios ranging
584 from 0.95-1.81 in the central HSM and 0.95-3.12 in the the southern HSM. Additionally,

585 $\sigma_3:S_v$ ratios of 0.6-1 are measured at depths above 650-700 m TVD, while 0.92-1 are
586 measured below this depth interval along the HSM. These stress magnitude results reveal that
587 across the central and southern HSM, S_{Hmax} is dominantly σ_1 , indicating a thrust to strike-slip
588 faulting regime. The observed dominant thrust to strike-slip faulting regime is consistent with
589 observed contractional tectonics in the HSM developed by the subduction of the Hikurangi
590 Plateau beneath the North Island (Barnes et al., 1998; Nicol & Beavan, 2003), and the strike-
591 slip faulting generated by forearc rotation of the East Coast (Beanland & Haines, 1998;
592 Litchfield et al., 2014; Nicol et al., 2007; Wallace et al., 2004).

593 Behboudi et al. (2022) report a dominant ENE-WSW shallow crust S_{Hmax} orientation within
594 the central HSM, and WNW-ESE or NW-SE S_{Hmax} orientations for the southern HSM
595 (Figure 1b). Considering $\sigma_1=S_{Hmax}$ along the HSM, observed S_{Hmax} orientations suggest the
596 contemporary maximum compressional stress switches from subparallel (ENE-WSW) to the
597 Hikurangi margin in the north and central HSM, to roughly perpendicular (WNW-ESE or
598 NW-SE) to the Hikurangi margin in the southern HSM. Based on our confirmation here that
599 $\sigma_1=S_{Hmax}$ along the HSM, it is likely that contemporary tectonics in the central HSM are
600 dominantly strike-slip, while in the southern HSM, more contractional tectonics may be
601 expected.

602 The NNE/NE striking faults in the central HSM, while currently inactive, express reverse
603 dip-slip components to them based on seismic survey data (Western Energy New Zealand,
604 2001). This tectonic slip is at odds with the contemporary fault strike-parallel σ_1 (S_{Hmax}). We
605 suggest here that these central HSM faults formed in an initially contractional stress state
606 such that $\sigma_3=S_v$, $\sigma_1=S_{Hmax}$ oriented NW-SE which would have been consistent with the NW-
607 SE component of Pacific-Australian plate motion. Overtime, this stress state changed from
608 this contractional state to the modern strike-slip/contractional/contractional-oblique stress
609 state ($\sigma_3:S_v=0.92-1$, $\sigma_1=S_{Hmax}$ oriented ENE-WSW).

610 This switch in σ_1 orientation overtime and along HSM strike may be explained by (a) long-
611 term clockwise rotation of the Hikurangi forearc (b) clockwise rotation of the Hikurangi
612 forearc in conjunction with high shallow crust overpressures and/or mechanical property
613 variations, and/or (c) along-strike variation in slip behavior in the HSM.

614 Clockwise rotation of the forearc, which accommodates the margin-parallel component of
615 oblique Pacific-Australian plate motion, drives strike-slip and/or normal faulting within the
616 onshore portion of the northern and central HSM, and transpressional faulting in the southern

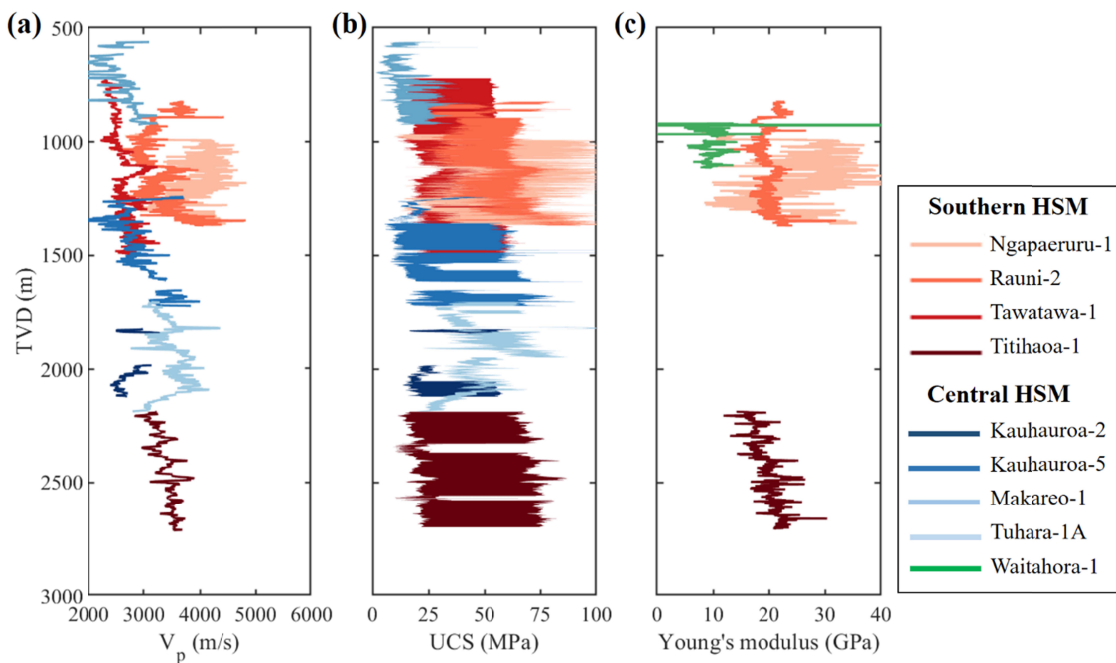
617 HSM (Figure 5, Fagereng & Ellis, 2009; Nicol et al., 2007; Wallace et al., 2004; Wallace,
618 Fagereng, & Ellis, 2012). Behboudi et al. (2022) suggest that this forearc rotation is likely
619 responsible for generating strike-slip stress state with ENE-WSW $S_{Hmax} = \sigma_1$ in the central
620 HSM, and contemporary contractional stress state with WNW-ESE/ NW-SE $S_{Hmax} = \sigma_1$ in the
621 southern HSM. However, our stress magnitude results of $\sigma_3 : S_v = 0.92-1$ and $\sigma_1 = S_{Hmax}$
622 leave a possibility for both strike-slip and contractional stress states to occur across both the
623 central and southern HSM due to poorly constrained UCS values used in this study, a
624 limitation of the study that could be restricted by laboratory rock strength testing of both
625 onshore and offshore HSM lithologies.

626 The northern and central HSM have high P_p based on borehole data (Burgreen-Chan et al.,
627 2016; D. Darby & Funnell, 2001), magnetotellurics (Heise et al., 2019), and seismic
628 tomography (Bassett et al., 2014; Eberhart-Phillips et al., 2017). Overpressure reduces the
629 effective normal stress on fault planes, meaning that the existing NNE/NE striking faults in
630 this region will be able to slip at lower shear stresses. Therefore, as the result of this
631 overpressure, these faults could be less stable, allowing the hangingwall of upper plate faults
632 to move more easily in response to NE-SW forces raised from forearc rotation. In this
633 scenario, forces raised from forearc rotation were able to alter stress state overtime from $\sigma_3 :$
634 $S_v = 1$ and $\sigma_1 = S_{Hmax}$ with NW-SE S_{Hmax} orientation, compatible with NW-SE component of
635 Pacific-Australian plate motion and old geological structures, to $\sigma_3 : S_v = 0.92-1$ and $\sigma_1 =$
636 S_{Hmax} with ENE-WSW S_{Hmax} orientation. Similar shallow, high overpressures are not
637 observed in the hangingwalls of upper plate faults in the onshore of the southern HSM.
638 Therefore it is possible that the NE-SW forces resulted from forearc rotation alone are
639 insufficient to exceed the fault shear resistance and change the orientation of σ_1 away from
640 the NW-SE component of Pacific-Australian plate motion, however they may have been high
641 enough to play a role in reducing σ_3 magnitudes to the point that they become $\leq S_v$,
642 resulting in a more transtensional tectonic regime overtime.

643 The mechanical properties of fault gauges and formations hosting faults (friction coefficient
644 and rock strength) can play a role in controlling upper plate tectonic stresses (Mantovani et
645 al., 2000; Marotta et al., 2002). Reiter (2021) investigated the impact of physical and elastic
646 parameter contrasts on S_{Hmax} orientation and proposed that contrasts in Young's modulus can
647 introduce S_{Hmax} rotations up to 78° , with larger stress rotations occurring within the softer
648 lithologies. Behboudi et al. (2022) proposed that basement uplift in the southern HSM may
649 introduce lateral geomechanical heterogeneities and variations in rock and sediment physical

650 properties along the HSM which may influence S_{Hmax} orientations. Such that clay and sand-
 651 siltstone sediments (Miocene to present), where our stress data are calculated, in the upper
 652 plate of the central HSM may geomechanically differ from clay and sand-siltstone sediments
 653 (Miocene to Cretaceous) in the onshore of the southern HSM. Therefore, we analyzed
 654 physical properties of aforementioned sediments and discovered that P-wave velocity (V_p),
 655 UCS ranges, and Young's modulus in the central HSM are lower than the onshore of southern
 656 HSM (Figure 10). In this scenario, S_{Hmax} orientations in the sediments of the central HSM,
 657 which have lower UCS and Young's modulus, could be easily reoriented in response to long-
 658 term forces such as forearc rotation compared to southern HSM. This theory, however, does
 659 not explain why the offshore boreholes in the southern HSM have not reoriented in response
 660 to long-term forearc rotation forces, while having comparable V_p , UCS range, and Young's
 661 Modulus to the boreholes in the central HSM.

662



663

664 **Figure 10.** Graph shows (a) p-wave velocity, (b) rock strength (UCS), and (c) Young's modulus in
 665 clay and sand-siltstone sediments as a function of depth across the central and southern HSM.

666

667 This along-strike variation in contemporary stress state is spatially consistent with north to
 668 south variation in slip behavior along the Hikurangi subduction interface (**Figure 1a**). In the
 669 northern and central HSM, the subduction interface is largely creeping and experiences
 670 shallow (<15 km), episodic slow slip events that extend offshore and possibly to the trench.
 671 At the southern HSM the plate interface is strongly interseismically locked to ~30 km depth,
 and is currently accumulating elastic strain in the surrounding crust (Wallace, 2020). Some

672 studies suggest that SSEs can release the amount of energy equivalent to a M_w 6.5–8
673 earthquakes (Dixon et al., 2014; Wallace, Beavan, et al., 2012). In the central HSM the
674 recurring SSEs and frequent earthquakes may release energy overtime such that the normal to
675 shear stress ratio on pre-existing faults has changed in a way that make it easier to slip in
676 response to forces deriving from long-term forearc rotation. While stress accumulation due to
677 locked nature of the southern HSM, don't allow the normal to shear stress ratio change
678 considerably on the existing NNE/NE striking compressional faults and make it difficult for
679 the hanging wall of these faults to slip in response to forearc rotation forces; therefore stress
680 state has not changed overtime in the southern HSM. However, the static stress drop of SSEs
681 is estimated to range 0.01–1.0 MPa (Gao et al., 2012). Given that the contemporary σ_3 :
682 $S_v \approx 0.95$ and $S_v - \sigma_3$ ranges between 0-3 MPa (for depths less than 3 km), these SSEs should
683 have existed in the central HSM for more than 20 years such that they were able to release
684 energy in order of 3 MPa (for depths less than 3 km) to change the initial $\sigma_3 : S_v = 1$ to the
685 contemporary $\sigma_3 : S_v = 0.92-1$ and reorient the S_{Hmax} orientation from NW-SE to ENE-WSW
686 in this region. However, further research and modeling are required to determine and quantify
687 the initial stress state and whether the amount of stress released during SSEs in the central
688 HSM was sufficient to support such a theory.

689 **5.2 Extensional tectonics within the HSM forearc**

690 There are locales in the central and southern HSM where stress magnitude determination
691 suggests a normal faulting regime ($\sigma_3 : S_v < 1$ and $0 \leq A_\phi \leq 1$). Also $\sigma_3 : S_v < 1$ where σ_3
692 calculated from LOT data is observed for 13 tests conducted at depth intervals anywhere
693 from ≈ 102 to 3611 m TVD in northern and central HSM boreholes (Table 1), and from 3
694 tests at depth intervals of $\approx 357-1586$ m TVD in southern HSM boreholes (Table 1). Several
695 factors can result in localized normal faulting regime at subduction margins including 1)
696 uncertainties in calculated UCS values and/or σ_3 magnitudes used to determine stress states
697 in this study, 2) the presence of local, active normal faults, and 3) fluctuations in stress
698 magnitudes modulated by seismic cycles.

699 **5.2.1. Uncertainties in calculated UCS values and σ_3 magnitudes**

700 Estimations of S_{Hmax} magnitudes are highly sensitive to the UCS values used, particularly
701 when UCS is determined from empirical relationships not constrained by laboratory testing
702 (Zoback, 2007). Due to lack of direct UCS data in this region, and a lack of empirical
703 relationships for the formations of this region to determine UCS from other rock properties,

704 this study relied on the use of a range of empirical relationships developed elsewhere to
705 generate a low and high limit for UCS at the HSM. These UCS ranges were then used to
706 generate the lowest and highest limits of S_{Hmax} magnitude. When the lowest limit of UCS is
707 used it can result in a potentially extensional stress state such that $S_{hmin} \approx S_{Hmax} \leq S_v$. As such,
708 the uncertainty in calculated UCS values, and the resulting potential errors it can introduce
709 into a stress model for the HSM, highlight the importance of dedicated laboratory tests for
710 developing robust empirical relationships for UCS in the HSM region, and subduction
711 regions like this, where stress is a critical geological consideration for hazard and resource
712 management.

713 Inaccuracy involved in LOT measurements (section 3.3) along with the lack of detail reported
714 on LOT results introduces an unknown level of uncertainty on estimated σ_3 magnitudes, and
715 hence on estimated $\sigma_3:S_v$ ratios using this data. Additionally, lack of LOT data along each
716 borehole necessitates the estimation of σ_3 profiles from the average $\sigma_3:S_v = 0.95$, which also
717 carries uncertainty. As a result, we recognize the potential impact this has on calculations of
718 S_{Hmax} magnitudes here, as well as on any interpretations of regional stress state and tectonics.
719 To investigate the potential effect of σ_3 uncertainties on S_{Hmax} calculations, we use both the
720 lower and upper limits of σ_3 values calculated from $\sigma_3:S_v = 0.92-1$, BO widths, and the lower
721 and upper boundary of UCS values. This analysis reveals that the σ_3 magnitude uncertainties
722 at the scale explored here have little influence on S_{Hmax} magnitude calculations (± 3.5 Mpa)
723 and hence do not change our findings about the stress regime and tectonics within the HSM
724 (blue areas in Figure 3; Figure 7b,c; Figure 9a,b).

725 **5.2.2 Presence of active normal faults**

726 Extensional structures are common within the overriding plate of many subduction margins
727 (Loveless et al., 2010; Moore et al., 2013). Normal faults in subduction zones are often
728 attributed to gravitational instabilities associated with subduction erosions and subsidence,
729 density imbalances produced by forearc uplifts, strain releases during earthquake cycles, and
730 flexural rigidity of the subduction interface (Barnes & Nicol, 2004; Collot et al., 1996;
731 Loveless et al., 2005; Park et al., 2002; Sacks et al., 2013). Within the HSM, localized
732 extensional stresses within the overriding plate are suggested to result from processes such as
733 slab rollback, forearc rotation (Nicol et al., 2007; Wallace et al., 2004), subduction erosion
734 and related subsidence, gravitational collapse due to forearc uplift, and growth of bending-

735 moment faults (Barnes & Nicol, 2004; Chanier et al., 1999; Upton et al., 2003; Walcott,
736 1987; Wallace, Fagereng, et al., 2012).

737 The σ_3 magnitude of 8.4 MPa measured from LOP in borehole Tuhara-1/1A (590.8 m TVD;
738 Table 1) is lower than σ_3 values of 8.95 MPa estimated from normal faulting failure with a
739 friction coefficient of 0.6 (Equation 7). This lower σ_3 magnitude may indicate there are active
740 normal faults at this depth along this borehole. In addition, borehole Tuhara-1A is located
741 within the Tuhara anticline structure, formed by contractional stresses resulting from two
742 blind thrust faults beneath the structure (Western Energy New Zealand, 1999). Our stress
743 magnitudes and HRT's (2000) analysis suggests that the Tuhara structure currently
744 experiences a dominant strike-slip faulting regime ($S_{hmin} \leq S_v \leq S_{Hmax}$; $1 \leq A_\phi \leq 2$) along the
745 majority of the borehole, interspersed with intervals of normal faulting regime ($S_{hmin} \leq S_{Hmax}$
746 $\leq S_v$; $0 \leq A_\phi < 1$) mainly within the 1700-1820 m and 2100-2145 m TVD depth interval
747 (Figure 3). A prominent feature of the Tuhara structure, as indicated by seismic reflection
748 profiles, is observation of relatively short steep east- and west-dipping normal faults
749 throughout Pliocene and Miocene successions (Western Energy New Zealand, 1999; Barnes
750 et al., 2002). Accordingly, we relate the appearance of normal stress states in our data to the
751 normal structures that develop as part of the larger compressional structural architecture of
752 this borehole site, and not due to the previously discussed uncertainties in the calculated UCS
753 and/or σ_3 magnitude values. This could particularly be the case where both the calculated
754 lower and upper limit of S_{Hmax} magnitudes are less than S_v (for example at 1700-1820 mTVD
755 in Tuhara-1A; Figure 3).

756 **5.2.3. Stress field fluctuations modulated by seismic cycling**

757 Fluctuations in stress magnitudes can be caused by seismic cycling. It has been reported that
758 earthquake events generate stress drops of 0.01 to 100 MPa, depending on the rheology,
759 roughness of fault, geometry of slip area, and heterogeneous stress fields (Allmann &
760 Shearer, 2009; Baltay et al., 2011; Candela et al., 2011; Cocco et al., 2016; Oth et al., 2010).
761 The observation of localized normal faulting regimes in the HSM may be related to seismic
762 cycling in the region. The normal faulting regimes observed along central HSM boreholes
763 Kauhauroa-2 (1980-2075 m TVD), Kauhauroa-5 (1330-1345 m TVD), and Tuhara-1A (1700-
764 1820 m TVD) occur where S_{Hmax} and S_v are very similar and are greater than S_{hmin} (Figure 3,
765 Figure 7b & 7c). In such stress state scenarios, a post-seismic stress drop of only a few MPa
766 after great earthquakes or frequent moderate earthquakes in the HSM region could perturb the

767 delicately balanced stress magnitudes surrounding these boreholes, switching $\sigma_1 = S_{Hmax}$ to
768 $\sigma_1 = S_v$ i.e. from a reverse/strike-slip to a normal stress state, accompanied by small rotations
769 in the S_{Hmax} orientation.

770 **6 Conclusions**

771 This work represents the first comprehensive determination of the *in-situ* stress state of the
772 HSM margin using available borehole data. We found a $\sigma_3 : S_v = 0.6-1$ at depths above 650-
773 700 m TVD, while $\sigma_3 : S_v = 0.92-1$ below this depth interval along the HSM. Stress
774 magnitudes calculated from borehole data indicate that the $S_{Hmax} : S_v$ ratios ranging from 0.95-
775 1.81 in the central HSM and 0.95-3.12 in the the southern HSM. These principal stress
776 magnitude results indicate a $\sigma_1 = S_{Hmax}$ and a thrust to strike-slip faulting regime across the
777 both central and southern HSM. The pre-existing NNE/NE striking reverse faults along the
778 both central and southern HSM infer that stress regime was initially in a contractional state
779 such that $\sigma_3 : S_v = 1$, $\sigma_1 = S_{Hmax}$, and a dominant NW-SE S_{Hmax} , consistent with NW-SE
780 component of Pacific-Australian plate motion. Taking contemporary stress state of $\sigma_1 = S_{Hmax}$
781 and ENE-WSW S_{Hmax} orientation and initial stress state into account in the central HSM,
782 these observations suggest that the compressional regime has shifted from subparallel to
783 perpendicular to the NW-SE Hikurangi convergence direction overtime in this region.
784 Variation of the central HSM stress state overtime may result from forces arising from
785 Hikurangi forearc rotation either by itself or facilitated by the upper plate, shallow, high
786 overpressures in the central HSM. Along-strike variation in slip behavior may also play a role
787 by releasing stress overtime due to SSEs and frequent earthquakes, hence changing the stress
788 state in the central HSM, while in the southern HSM, the modern WNW-ESE/ NW-SE σ_1
789 (S_{Hmax}) remains subparallel to NW-SE Hikurangi convergence direction overtime, may reflect
790 the interseismic locked nature of the plate interface. Finally, stress determination highlights
791 localized normal stress states within the HSM forearc interpreted to be due to processes such
792 as the presence of localized active normal faults or fluctuations in stress magnitudes
793 modulated by seismic cycles. The determination of HSM *in-situ* stresses in this study will
794 provide an invaluable tool for improving our understanding of the stability of upper plate
795 faults and will facilitate more quantitative efforts to assess the seismic hazard potential of the
796 HSM that will support of disaster risk reduction plans.

797 **Acknowledgments**

798 This publication has emanated from research conducted with the financial support of Science
799 Foundation Ireland (SFI) under Grant Number 17/RC-PhD/3481 and co funded by
800 Geological survey of Ireland (GSI). The authors would like to thank the New Zealand
801 Petroleum and Minerals group (NZPM) within the Ministry for Business, Innovation and
802 Employment (MBIE) for providing access to borehole data and supporting materials for this
803 study. We also thank Schlumberger for providing academic licenses for Techlog 2018.1 to
804 University College Dublin and University of Liverpool. We thank MathWorks for providing
805 academic licenses for MATLAB to University College Dublin. We thank Esri for providing
806 the academic license of ArcGIS Pro to University College Dublin. For the purpose of Open
807 Access, the author has applied a CC BY public copyright license to any Author Accepted
808 Manuscript version arising from this submission.

809 **Data Availability Statement**

810 This research used data provided by the New Zealand Petroleum and Minerals group
811 (NZPM) within the Ministry for Business, Innovation and Employment (MBIE). The
812 borehole image logs used in this paper can accessed through MBIE's online free database
813 (<https://data.nzpam.govt.nz/GOLD/system/mainframe.asp>). Borehole breakout measurements
814 presented in this study can be accessed at
815 https://github.com/BehboudiEffatGeo/StressCharacterization_HSM.git and
816 <https://doi.org/10.5281/zenodo.7450966>.

817

818 **References**

- 819 Aadnoy, B. S. (1990). Inversion technique to determine the in-situ stress field from fracturing
820 data. *Journal of Petroleum Science and Engineering*, 4(2), 127–141.
- 821 Addis, M. A., Hanssen, T. H., Yassir, N., Willoughby, D. R., & Enever, J. (1998). A
822 Comparison Of Leak-Off Test And Extended Leak-Off Test Data For Stress Estimation.
823 In *SPE/ISRM Rock Mechanics in Petroleum Engineering* (p. SPE-47235-MS).
824 <https://doi.org/10.2118/47235-MS>
- 825 Allmann, B. P., & Shearer, P. M. (2009). Global variations of stress drop for moderate to
826 large earthquakes. *Journal of Geophysical Research: Solid Earth*, 114(B01310).
827 <https://doi.org/10.1029/2008JB005821>
- 828 Ando, R., Takeda, N., & Yamashita, T. (2012). Propagation dynamics of seismic and
829 aseismic slip governed by fault heterogeneity and Newtonian rheology. *Journal of*
830 *Geophysical Research B: Solid Earth*, 117(B11308).
831 <https://doi.org/10.1029/2012JB009532>
- 832 Audet, P., Bostock, M. G., Christensen, N. I., & Peacock, S. M. (2009). Seismic evidence for
833 overpressured subducted oceanic crust and megathrust fault sealing. *Nature*, 457(7225),
834 76–78. <https://doi.org/10.1038/nature07650>
- 835 Baltay, A., Ide, S., Prieto, G., & Beroza, G. (2011). Variability in earthquake stress drop and
836 apparent stress. *Geophysical Research Letters*, 38(6).
837 <https://doi.org/10.1029/2011GL046698>

- 838 Barnes, P. M., Lamarche, G., Bialas, J., Henrys, S., Pecher, I., Netzeband, G. L., Greinert, J.,
839 Mountjoy, J. J., Pedley, K., & Crutchley, G. (2010). Tectonic and geological framework
840 for gas hydrates and cold seeps on the Hikurangi subduction margin, New Zealand.
841 *Marine Geology*, 272(1–4), 26–48. <https://doi.org/10.1016/j.margeo.2009.03.012>
- 842 Barnes, P. M., Lpinay, M. De, Collot, J. Y., Delteil, J., & Audru, J.-C. (1998). Strain
843 partitioning in the transition area between oblique subduction and continental collision,
844 Hikurangi margin. *Tectonics*, 17(4), 534–557.
- 845 Barnes, P. M., & Nicol, A. (2004). Formation of an active thrust triangle zone associated with
846 structural inversion in a subduction setting, eastern New Zealand. *Tectonics*, 23(1), 1–
847 25. <https://doi.org/10.1029/2002TC001449>
- 848 Barton, C. A., Zoback, M. D., & Burns, K. L. (1988). In-situ stress orientation and magnitude
849 at the Fenton Geothermal Site, New Mexico, determined from wellbore breakouts.
850 *Geophysical Research Letters*, 15(5), 467–470.
- 851 Bassett, D., Sutherland, R., & Henrys, S. (2014). Slow wavespeeds and fluid overpressure in
852 a region of shallow geodetic locking and slow slip, Hikurangi subduction margin, New
853 Zealand. *Earth and Planetary Science Letters*, 389, 1–13.
854 <https://doi.org/10.1016/j.epsl.2013.12.021>
- 855 Beanland, S., & Haines, J. (1998). The kinematics of active deformation in the North Island,
856 New Zealand, determined from geological strain rates. *New Zealand Journal of Geology
857 and Geophysics*, 41(4), 311–323. <https://doi.org/10.1080/00288306.1998.9514813>
- 858 Beavan, J., Tregoning, P., Bevis, M., Kato, T., & Meertens, C. (2002). Motion and rigidity of
859 the Pacific Plate and implications for plate boundary deformation. *Journal of
860 Geophysical Research: Solid Earth*, 107(B10), ETG 19-1-ETG 19-15.
861 <https://doi.org/10.1029/2001jb000282>
- 862 Beetham, R. D., McSaveney, M. J., & Read, S. A. L. (2018). Four extremely large landslides
863 in New Zealand. In *Landslides* (pp. 97–102). Routledge.
- 864 Behboudi, E., Mcnamara, D. D., Lokmer, I., Wallace, L. M., & Saffer, D. M. (2022). Spatial
865 Variation of Shallow Stress Orientation Along the Hikurangi Subduction Margin :
866 Insights From In-Situ Borehole Image Logging *Journal of Geophysical Research : Solid
867 Earth*. *Journal of Geophysical Research : Solid Earth*, 127.
868 <https://doi.org/10.1029/2021JB023641>
- 869 Bell, J. S. (1996). Petro Geoscience 1. In situ stresses in sedimentary rocks (part 1):
870 measurement techniques. *Geoscience Canada*.
- 871 Bell, J. S. (2003). Practical methods for estimating in situ stresses for borehole stability
872 applications in sedimentary basins. *Journal of Petroleum Science and Engineering*,
873 38(3–4), 111–119. [https://doi.org/10.1016/S0920-4105\(03\)00025-1](https://doi.org/10.1016/S0920-4105(03)00025-1)
- 874 Bell, J. S., & Gough, D. I. (1979). Northeast-southwest compressive stress in Alberta
875 evidence from oil wells. *Earth and Planetary Science Letters*, 45(2), 475–482.
876 [https://doi.org/10.1016/0012-821X\(79\)90146-8](https://doi.org/10.1016/0012-821X(79)90146-8)
- 877 Brodsky, E. E., Mori, J. J., Anderson, L., Chester, F. M., Conin, M., Dunham, E. M., Eguchi,
878 N., Fulton, P. M., Hino, R., Hirose, T., Ikari, M. J., Saffer, D. M., Saito, S., Sample, J.,
879 Sun, T., Toczko, S., & Ujiie, K. (2020). The State of Stress on the Fault Before, During
880, and After a Major Earthquake. *Annual Review of Earth and Planetary Sciences*,
881 48(May). <https://doi.org/10.1146/annurev-earth-053018-060507>
- 882 Brodsky, E. E., Saffer, D., Fulton, P., Chester, F., Conin, M., Huffman, K., Moore, J. C., &
883 Wu, H.-Y. (2017). The postearthquake stress state on the Tohoku megathrust as
884 constrained by reanalysis of the JFAST breakout data. *Geophysical Research Letters*,
885 44, 8294–8302. <https://doi.org/10.1002/2017GL074027>
- 886 Brudy, M., & Zoback, M. D. (1999). Drilling-induced tensile wall-fractures: implications for
887 determination of in-situ stress orientation and magnitude. *International Journal of Rock*

- 888 *Mechanics and Mining Sciences*, 36(2), 191–215.
- 889 Burgreen-Chan, B., Meisling, K. E., & Graham, S. (2016). Seismic reflection character of the
890 Hikurangi subduction interface, New Zealand, in the region of repeated Gisborne slow
891 slip events. *Basin Research*, 28(4), 536–567. <https://doi.org/10.1111/bre.12121>
- 892 Candela, T., Renard, F., Bouchon, M., Schmittbuhl, J., & Brodsky, E. E. (2011). Stress Drop
893 during Earthquakes: Effect of Fault Roughness Scaling. *Bulletin of the Seismological*
894 *Society of America*, 101(5), 2369–2387. <https://doi.org/10.1785/0120100298>
- 895 Chang, C., McNeill, L. C., Moore, J. C., Lin, W., Conin, M., & Yamada, Y. (2010). In situ
896 stress state in the Nankai accretionary wedge estimated from borehole wall failures.
897 *Geochemistry, Geophysics, Geosystems*, 11(12), 1–17.
898 <https://doi.org/10.1029/2010GC003261>
- 899 Chang, C., Zoback, M. D., & Khaksar, A. (2006). Empirical relations between rock strength
900 and physical properties in sedimentary rocks. *Journal of Petroleum Science and*
901 *Engineering*, 51(3–4), 223–237. <https://doi.org/10.1016/j.petrol.2006.01.003>
- 902 Chanier, F., Ferriere, J., & Angelier, J. (1999). Extensional deformation across an active
903 margin, relations with subsidence, uplift, and rotations: The Hikurangi subduction, New
904 Zealand. *Tectonics*, 18(5), 862–876.
- 905 Cocco, M., Tinti, E., & Cirella, A. (2016). On the scale dependence of earthquake stress drop.
906 *Journal of Seismology*, 20(4), 1151–1170. <https://doi.org/10.1007/s10950-016-9594-4>
- 907 Collot, J. Y., Delteil, J., Lewis, K. B., Davy, B., Lamarche, G., Audru, J. C., Barnes, P.,
908 Chanier, F., Chaumillon, E., Lallemand, S., De Lepinay, B. M., Orpin, A., Pelletier, B.,
909 Sosson, M., Toussaint, B., & Uruski, C. (1996). From oblique subduction to intra-
910 continental transpression: Structures of the southern Kermadec-Hikurangi margin from
911 multibeam bathymetry, side-scan sonar and seismic reflection. *Marine Geophysical*
912 *Research*, 18(2–4), 357–381. <https://doi.org/10.1007/BF00286085>
- 913 Couzens-Schultz, B. A., & Chan, A. W. (2010). Stress determination in active thrust belts:
914 An alternative leak-off pressure interpretation. *Journal of Structural Geology*, 32(8),
915 1061–1069. <https://doi.org/10.1016/j.jsg.2010.06.013>
- 916 Darby, D., & Ellis, S. (2001). Evaluating Overpressure in Compressional Regimes Using
917 Geomechanical Modeling. *PESA Eastern Australian Basins Symposium*, 613–620.
- 918 Darby, D., & Funnell, R. H. (2001). Overpressure associated with a convergent plate margin:
919 East Coast Basin, New Zealand. *Petroleum Geoscience*, 7(3), 291–299.
920 <https://doi.org/10.1144/petgeo.7.3.291>
- 921 Darby, David, & Funnell, R. H. (2001). Overpressure associated with a convergent plate
922 margin : East Coast Basin , New Zealand. *Petroleum Geoscience*, 7(3), 291–299.
923 [https://doi.org/Mcnamara, D. D., Behboudi, E., Wallace, L., Saffer, D., Cook, A. E., & Fagereng, A. \(2021\). Variable In Situ Stress Orientations Across the Northern Hikurangi Subduction Margin Geophysical Research Letters. *Petroleum Geoscience*, 7\(3\), 291–
924 299. <https://doi.org/https://doi.org/10.1144/petgeo.7.3.291>](https://doi.org/Mcnamara, D. D., Behboudi, E., Wallace, L., Saffer, D., Cook, A. E., & Fagereng, A. (2021). Variable In Situ Stress Orientations Across the Northern Hikurangi Subduction Margin Geophysical Research Letters. Petroleum Geoscience, 7(3), 291–299. https://doi.org/https://doi.org/10.1144/petgeo.7.3.291)
- 925 299. <https://doi.org/https://doi.org/10.1144/petgeo.7.3.291>
- 926
- 927 Davy, B. (1992). The influence of subducting plate buoyancy on subduction of the
928 Hikurangi-Chatham Plateau beneath the North Island, New Zealand. In *Geology and*
929 *geophysics of continental margins*.
- 930 Davy, B., Hoernle, K., & Werner, R. (2008). Hikurangi Plateau: Crustal structure, rifted
931 formation, and Gondwana subduction history. *Geochemistry, Geophysics, Geosystems*,
932 9(7). <https://doi.org/10.1029/2007GC001855>
- 933 Delvaux, D., Moeys, R., Stapel, G., Petit, C., Levi, K., Miroshnichenko, A., Ruzhich, V., &
934 San, V. (1997). Paleostress reconstructions and geodynamics of the Baikal region ,
935 Central Asia , Part 2 . Cenozoic rifting. *Tectonophysics*, 282(1–4), 1–38.
- 936 Dixon, T. H., Jiang, Y., Malservisi, R., McCaffrey, R., Voss, N., Protti, M., & Gonzalez, V.
937 (2014). Earthquake and tsunami forecasts: Relation of slow slip events to subsequent

938 earthquake rupture. *Proceedings of the National Academy of Sciences of the United*
939 *States of America*, 111(48), 17039–17044. <https://doi.org/10.1073/pnas.1412299111>

940 Doser, D. I., & Webb, T. H. (2003). Source parameters of large historical (1917-1961)
941 earthquakes, North Island, New Zealand. *Geophysical Journal International*, 152, 795–
942 832. <https://doi.org/10.1046/j.1365-246X.2003.01895.x>

943 Downes, G. L. (2006). The 1904 Ms6.8 Mw7.0-7.2 Cape Turnagain, New Zealand,
944 earthquake. *Bulletin of the New Zealand Society for Earthquake Engineering*, 39(4),
945 183–207. <https://doi.org/10.5459/bnzsec.39.4.183-207>

946 Dutta, N. C., Bachrach, R., & Mukerji, T. (2021). *Quantitative Analysis of Geopressure for*
947 *Geoscientists and Engineers*. Cambridge University Press.
948 <https://doi.org/10.1017/9781108151726>

949 Eberhart-Phillips, D., Bannister, S., & Reyners, M. (2017). Deciphering the 3-D distribution
950 of fluid along the shallow Hikurangi subduction zone using P- and S-wave attenuation.
951 *Geophysical Journal International*, 211(2), 1032–1045.
952 <https://doi.org/10.1093/gji/ggx348>

953 Evanzia, D., Wilson, T., Savage, M. K., & Hamish, H. (2017). Stress Orientations in a
954 Locked Subduction Zone at the Southern Hikurangi Margin, New Zealand. *Journal of*
955 *Geophysical Research : Solid Earth*, 122, 7895–7911.
956 <https://doi.org/10.1002/2017JB013998>

957 Fagereng, A., & Ellis, S. (2009). On factors controlling the depth of interseismic coupling on
958 the Hikurangi subduction interface, New Zealand. *Earth and Planetary Science Letters*,
959 278, 120–130. <https://doi.org/10.1016/j.epsl.2008.11.033>

960 Gao, H., Schmidt, D. A., & Weldon, R. J. (2012). Scaling relationships of source parameters
961 for slow slip events. *Bulletin of the Seismological Society of America*, 102(1), 352–360.
962 <https://doi.org/10.1785/0120110096>

963 Gardner, G. H. F., Gardner, L. W., & Gregory, A. (1974). Formation velocity and density—
964 The diagnostic basics for stratigraphic traps. *Geophysics*, 39(6), 770–780.

965 Grapes, R., & Downes, G. (1997). The 1855 Wairarapa, New Zealand, earthquake. *Bulletin of*
966 *the New Zealand Society for Earthquake Engineering*, 30(4), 271–368.
967 <https://doi.org/10.5459/bnzsec.30.4.271-368>

968 Griffin, A. G. (2019). Subsurface SHMAX determined from a borehole image log, onshore
969 southern East Coast Basin, New Zealand. *New Zealand Journal of Geology and*
970 *Geophysics*, 62(2), 273–290. <https://doi.org/10.1080/00288306.2019.1570946>

971 Griffin, A. G., Bland, K. J., Morgans, H. E. G., Strogen, D. P., Griffin, A. G., Bland, K. J.,
972 Morgans, H. E. G., Strogen, D. P., Bland, K. J., Morgans, H. E. G., & Strogen, D. P.
973 (2021). A multifaceted study of the offshore Titihaoa-1 drillhole and a Neogene
974 accretionary slope basin , Hikurangi subduction margin. *New Zealand Journal of*
975 *Geology and Geophysics*, 0(0), 1–26. <https://doi.org/10.1080/00288306.2021.1932527>

976 Gunter, J. M., & Moore, C. V. (1986). Improved Use of Wireline Testers for Reservoir
977 Evaluation. In *International Meeting on Petroleum Engineering* (p. SPE-14063-MS).
978 <https://doi.org/10.2118/14063-MS>

979 Hardebeck, J. L. (2012). *Coseismic and postseismic stress rotations due to great subduction*
980 *zone earthquakes*. 39(October), 1–6. <https://doi.org/10.1029/2012GL053438>

981 Hardebeck, J. L., & Okada, T. (2018). Temporal Stress Changes Caused by Earthquakes: A
982 Review. *Journal of Geophysical Research : Solid Earth*, 123, 1350–1365.
983 <https://doi.org/10.1002/2017JB014617>

984 Heidbach, O., Rajabi, M., Cui, X., Fuchs, K., Müller, B., Reinecker, J., Reiter, K., Tingay,
985 M., Wenzel, F., Xie, F., Ziegler, M. O., Zoback, M. Lou, & Zoback, M. (2018). The
986 World Stress Map database release 2016: Crustal stress pattern across scales.
987 *Tectonophysics*, 744(July), 484–498. <https://doi.org/10.1016/j.tecto.2018.07.007>

- 988 Heise, W., Ogawa, Y., Bertrand, E. A., Caldwell, T. G., Yoshimura, R., Ichihara, H., Bennie,
989 S. L., Seki, K., Saito, Z., Matsunaga, Y., Suzuki, A., Kishita, T., & Kinoshita, Y. (2019).
990 Electrical resistivity imaging of the inter-plate coupling transition at the Hikurangi
991 subduction margin, New Zealand. *Earth and Planetary Science Letters*, *524*, 115710.
992 <https://doi.org/10.1016/j.epsl.2019.115710>
- 993 Huffman, K. A., & Saffer, D. M. (2016). In situ stress magnitudes at the toe of the Nankai
994 Trough Accretionary Prism, offshore Shikoku Island, Japan. *Journal of Geophysical
995 Research : Solid Earth*, *121*, 1202–1217. <https://doi.org/10.1002/2015JB012415>
- 996 Ito, Y., & Obara, K. (2006). *Very low frequency earthquakes within accretionary prisms are
997 very low stress-drop earthquakes*. 33(January), 1–4.
998 <https://doi.org/10.1029/2006GL025883>
- 999 Jaeger, J. C., Cook, N. G. W., & Zimmerman, R. (2009). *Fundamentals of rock mechanics*.
1000 John Wiley & Sons.
- 1001 Kodaira, S., Iidaka, T., Kato, A., Park, J. O., Iwasaki, T., & Kaneda, Y. (2004). High pore
1002 fluid pressure may cause silent slip in the Nankai Trough. *Science*, *304*(5675), 1295–
1003 1298. <https://doi.org/10.1126/science.1096535>
- 1004 Kurzawski, R. M., Niemeijer, A. R., Stipp, M., Charpentier, D., Behrmann, J. H., & Spiers,
1005 C. J. (2018). Frictional Properties of Subduction Input Sediments at an Erosive
1006 Convergent Continental Margin and Related Controls on Décollement Slip Modes: The
1007 Costa Rica Seismogenesis Project. *Journal of Geophysical Research: Solid Earth*,
1008 *123*(10), 8385–8408. <https://doi.org/10.1029/2017JB015398>
- 1009 Lange, W. P. de, & Moon, V. G. (2004). Estimating earthquake and landslide tsunami hazard
1010 for the New Zealand coast. *Bulletin of the New Zealand Society for Earthquake
1011 Engineering*, *37*(2), 62–69. <https://doi.org/10.5459/bnzsee.37.2.62-69>
- 1012 Langridge, R. M., Ries, W. F., Litchfield, N. J., Villamor, P., Dissen, R. J. Van, Barrell, D. J.
1013 A., Rattenbury, M. S., Heron, D. W., Haubrock, S., Townsend, D. B., Lee, J. M.,
1014 Berryman, K. R., Nicol, A., Cox, S. C., & Stirling, M. W. (2016). The New Zealand
1015 Active Faults Database. *New Zealand Journal of Geology and Geophysics ISSN:*, *59*(1),
1016 86–96. <https://doi.org/10.1080/00288306.2015.1112818>
- 1017 Lawrence, M. J. F. (2018). Structural and Sedimentological Interpretation of Well Data from
1018 the Wairoa Area , North Island , New Zealand. *GNS Science Report 2018/28, August*, 1–
1019 76. <https://doi.org/10.21420/G23W81>
- 1020 Lee, J., Swarbrick, R., & Connor, S. O. (2022). Kicks and their significance in pore pressure
1021 prediction. *Petroleum Geoscience*, *28*. <https://doi.org/10.1144/petgeo2021-061>
- 1022 Litchfield, N. J., Van Dissen, R., Sutherland, R., Barnes, P. M., Cox, S. C., Norris, R.,
1023 Beavan, R. J., Langridge, R., Villamor, P., Berryman, K., Stirling, M., Nicol, A.,
1024 Nodder, S., Lamarche, G., Barrell, D. J. A., Pettinga, J. R., Little, T., Pondard, N.,
1025 Mountjoy, J. J., & Clark, K. (2014). A model of active faulting in New Zealand. *New
1026 Zealand Journal of Geology and Geophysics*, *57*(1), 32–56.
1027 <https://doi.org/10.1080/00288306.2013.854256>
- 1028 Liu, Y., & Rice, J. R. (2007). Spontaneous and triggered aseismic deformation transients in a
1029 subduction fault model. *Journal of Geophysical Research*, *112*(B09404).
1030 <https://doi.org/10.1029/2007JB004930>
- 1031 Loveless, J. P., Allmendinger, R. W., Pritchard, M. E., & González, G. (2010). Normal and
1032 reverse faulting driven by the subduction zone earthquake cycle in the northern Chilean
1033 fore arc. *Tectonics*, *29*(TC2001). <https://doi.org/10.1029/2009TC002465>
- 1034 Loveless, J. P., Hoke, G. D., Allmendinger, R. W., González, G., Isacks, B. L., & Carrizo, D.
1035 A. (2005). Pervasive cracking of the northern Chilean Coastal Cordillera: New evidence
1036 for forearc extension. *Geology*, *33*(12), 973–976. <https://doi.org/10.1130/G22004.1>
- 1037 Ltd., I.-P. E. (NZ). (2002). *Waingaromia-2 Well Completion Report*. Ministry of Economic

- 1038 Development New Zealand, Unpublished Open file Petroleum Report 2767.
- 1039 Ma, K. F., Chan, C. H., & Stein, R. S. (2005). Response of seismicity to Coulomb stress
1040 triggers and shadows of the 1999 Mw=7.6 Chi-Chi, Taiwan, earthquake. *Journal of*
1041 *Geophysical Research: Solid Earth*, 110(B05S19).
1042 <https://doi.org/10.1029/2004JB003389>
- 1043 Ma, Y. Z., & Holditch, S. A. (2015). Unconventional Oil and Gas Resources Handbook:
1044 Evaluation and Development. In *Unconventional Oil and Gas Resources Handbook:*
1045 *Evaluation and Development*. Gulf professional publishing.
1046 <https://doi.org/10.1016/C2014-0-01377-9>
- 1047 Mantovani, E., Viti, M., Albarello, D., Tamburelli, C., Babbucci, D., & Cenni, N. (2000).
1048 Role of kinematically induced horizontal forces in Mediterranean tectonics: insights
1049 from numerical modeling. *Journal of Geodynamics*, 30(3), 287–320.
1050 [https://doi.org/10.1016/S0264-3707\(99\)00067-8](https://doi.org/10.1016/S0264-3707(99)00067-8)
- 1051 Marotta, A. ., Bayer, U., Thybo, H., & Scheck, M. (2002). Origin of the regional stress in the
1052 North German basin: results from numerical modelling. *Tectonophysics*, 360(1–4), 245–
1053 264. [https://doi.org/10.1016/S0040-1951\(02\)00358-X](https://doi.org/10.1016/S0040-1951(02)00358-X)
- 1054 Mcnamara, D. D., Behboudi, E., Wallace, L., Saffer, D., Cook, A. E., & Fagereng, A. (2021).
1055 Variable In Situ Stress Orientations Across the Northern Hikurangi Subduction Margin
1056 Geophysical Research Letters. *Geophysical Research Letters*, 48.
1057 <https://doi.org/https://doi.org/10.1029/2020GL091707>
- 1058 McNamara, D. D., Behboudi, E., Wallace, L., Saffer, D., Cook, A. E., Fagereng, A.,
1059 Paganoni, M., Wu, H. Y., Kim, G., Lee, H., Savage, H. M., Barnes, P., Pecher, I.,
1060 LeVay, L. J., & Petronotis, K. E. (2021). Variable In Situ Stress Orientations Across the
1061 Northern Hikurangi Subduction Margin. *Geophysical Research Letters*, 48(5).
1062 <https://doi.org/10.1029/2020GL091707>
- 1063 Moore, G. F., Boston, B. B., Sacks, A. F., & Saffer, D. M. (2013). Analysis of normal fault
1064 populations in the Kumano Forearc Basin , Nankai Trough , Japan : 1 . Multiple
1065 orientations and generations of faults from 3-D coherency mapping. *Geochemistry,*
1066 *Geophysics, Geosystems*, 114, 1989–2002. <https://doi.org/10.1002/ggge.20119>
- 1067 Moos, D., & Zoback, M. D. (1990). Utilization of observations of well bore failure to
1068 constrain the orientation and magnitude of crustal stresses: application to continental,
1069 Deep Sea Drilling Project, and Ocean Drilling Program boreholes. *Journal of*
1070 *Geophysical Research*, 95(B6), 9305–9325. <https://doi.org/10.1029/JB095iB06p09305>
- 1071 Mountjoy, J. J., & Barnes, P. M. (2011). Active upper plate thrust faulting in regions of low
1072 plate interface coupling, repeated slow slip events, and coastal uplift: Example from the
1073 Hikurangi Margin, New Zealand. *Geochemistry, Geophysics, Geosystems*, 12(1), 1–26.
1074 <https://doi.org/10.1029/2010GC003326>
- 1075 Nicol, A., & Beavan, J. (2003). Shortening of an overriding plate and its implications for slip
1076 on a subduction thrust, central Hikurangi Margin, New Zealand. *Tectonics*, 22(6), n/a-
1077 n/a. <https://doi.org/10.1029/2003tc001521>
- 1078 Nicol, A., Mazengarb, C., Chanier, F., Rait, G., Uruski, C., & Wallace, L. (2007). Tectonic
1079 evolution of the active Hikurangi subduction margin, New Zealand, since the Oligocene.
1080 *Tectonics*, 26(4), 1–24. <https://doi.org/10.1029/2006TC002090>
- 1081 Oth, A., Bindi, D., Parolai, S., & Di Giacomo, D. (2010). Earthquake scaling characteristics
1082 and the scale-(in)dependence of seismic energy-to-moment ratio: Insights from KiK-net
1083 data in Japan. *Geophysical Research Letters*, 37(19).
1084 <https://doi.org/10.1029/2010GL044572>
- 1085 Park, J.-O., Tsuru, T., Kodaira, S., Cummins, P. R., & Kaneda, Y. (2002). Splay Fault
1086 Branching Along the Nankai Subduction Zone. *Science*, 297(5584), 1157–1160.
1087 <https://doi.org/10.1126/science.1074111>

- 1088 Pedley, K. L., Barnes, P. M., Pettinga, J. R., & Lewis, K. B. (2010). Seafloor structural
1089 geomorphic evolution of the accretionary frontal wedge in response to seamount
1090 subduction, Poverty Indentation, New Zealand. *Marine Geology*, 270(1–4), 119–138.
1091 <https://doi.org/10.1016/j.margeo.2009.11.006>
- 1092 Power, W. L., Reyners, M., & Wallace, L. M. (2008). Tsunami hazard posed by earthquakes
1093 on the Hikurangi subduction zone interface. In *GNS Science Consultancy Report*
1094 *2008/40* (Issue May).
- 1095 Reiter, K. (2021). Stress rotation – The impact and interaction of rock stiffness and faults.
1096 *Solid Earth*, 12(6), 1287–1307. <https://doi.org/10.5194/se-12-1287-2021>
- 1097 Riedel, M., Malinverno, A., Wang, K., Goldberg, D., & Guerin, G. (2016). Horizontal
1098 compressive stress regime on the northern Cascadia margin inferred from borehole
1099 breakouts. *Geochemistry, Geophysics, Geosystems*, 17(9), 3529–3545.
1100 <https://doi.org/10.1002/2016GC006443>
- 1101 Sacks, A., Saffer, D. M., & Fisher, D. (2013). Analysis of normal fault populations in the
1102 Kumano forearc basin, Nankai Trough, Japan: 2. Principal axes of stress and strain from
1103 inversion of fault orientations. *Geochemistry, Geophysics, Geosystems*, 14(6), 1973–
1104 1988. <https://doi.org/10.1002/ggge.20118>
- 1105 Saffer, D. M., & Wallace, L. M. (2015). The frictional, hydrologic, metamorphic and thermal
1106 habitat of shallow slow earthquakes. *Nature Publishing Group*, 8.
1107 <https://doi.org/10.1038/ngeo2490>
- 1108 Schellart, W. P., & Rawlinson, N. (2013). Global correlations between maximum magnitudes
1109 of subduction zone interface thrust earthquakes and physical parameters of subduction
1110 zones. *Physics of the Earth and Planetary Interiors*, 225, 41–67.
1111 <https://doi.org/10.1016/j.pepi.2013.10.001>
- 1112 Seeber, L., & Armbruster, J. G. (2000). Earthquakes as beacons of stress change. *Nature*,
1113 407(6800), 69–72. <https://doi.org/10.1038/35024055>
- 1114 Sibson, R. H. (1974). Frictional constraints on thrust, wrench and normal faults. *Nature*,
1115 249(5457), 542–544.
- 1116 Stein, R. S. (1999). The role of stress transfer in earthquake occurrence. *Nature*,
1117 402(December), 605–609.
- 1118 Townend, J., Sherburn, S., Arnold, R., Boese, C., & Woods, L. (2012). Three-dimensional
1119 variations in present-day tectonic stress along the Australia-Pacific plate boundary in
1120 New Zealand. *Earth and Planetary Science Letters*, 353–354, 47–59.
1121 <https://doi.org/10.1016/j.epsl.2012.08.003>
- 1122 Ujiie, K., & Kimura, G. (2014). Earthquake faulting in subduction zones: insights from fault
1123 rocks in accretionary prisms. *Progress in Earth and Planetary Science*, 1(7).
1124 <https://doi.org/10.1186/2197-4284-1-7>
- 1125 Upton, P., Koons, P. O., & Eberhart-phillips, D. (2003). Extension and partitioning in an
1126 oblique subduction zone , New Zealand : Constraints from three-dimensional numerical
1127 modeling. *Tectonics*, 22(6). <https://doi.org/10.1029/2002TC001431>
- 1128 Van Ruth, P. J., Hillis, R. R., & Swarbrick, R. E. (2002). Detecting overpressure using
1129 porosity-based techniques in the Carnarvon basin, Australia. *The APPEA Journal*, 42(1),
1130 559–569.
- 1131 Vavrycuk, V. (2015). Earthquake Mechanisms and Stress Field. In *Encyclopedia of*
1132 *Earthquake Engineering* (Issue January 2015). [https://doi.org/10.1007/978-3-642-](https://doi.org/10.1007/978-3-642-36197-5)
1133 [36197-5](https://doi.org/10.1007/978-3-642-36197-5)
- 1134 Vernik, L., & Zoback, M. D. (1992). Estimation of maximum horizontal principal stress
1135 magnitude from stress-induced well bore breakouts in the Cajon Pass scientific research
1136 borehole. *Journal of Geophysical Research: Solid Earth*, 97(B4), 5109–5119.
- 1137 Walcott, R. I. (1987). Geodetic Strain and the Deformational History of the North Island of

1138 New Zealand during the Late Cainozoic Author (s): R . I . Walcott Source :

1139 Philosophical Transactions of the Royal Society of London . Series A , Mathematical

1140 Published by : Royal Soci. *Philosophical Transactions of the Royal Society of London.*

1141 *Series A, Mathematical and Physical Sciences*, 321(1557), 163–181.

1142 <https://www.jstor.org/stable/37727>

1143 Wallace, L. M. (2020). Slow Slip Events in New Zealand. *Annual Review of Earth and*

1144 *Planetary Sciences*, 48, 175–203. <https://doi.org/10.1146/annurev-earth-071719-055104>

1145 Wallace, L. M., & Beavan, J. (2010). Diverse slow slip behavior at the Hikurangi subduction

1146 margin, New Zealand. *Journal of Geophysical Research: Solid Earth*, 115(12), 1–20.

1147 <https://doi.org/10.1029/2010JB007717>

1148 Wallace, L. M., Beavan, J., Bannister, S., & Williams, C. (2012). Simultaneous long-term

1149 and short-term slow slip events at the Hikurangi subduction margin, New Zealand:

1150 Implications for processes that control slow slip event occurrence, duration, and

1151 migration. *Journal of Geophysical Research B: Solid Earth*, 117(B11402).

1152 <https://doi.org/10.1029/2012JB009489>

1153 Wallace, L. M., Beavan, J., McCaffrey, R., & Darby, D. (2004). Subduction zone coupling

1154 and tectonic block rotations in the North Island, New Zealand. In *Journal of*

1155 *Geophysical Research: Solid Earth* (Vol. 109, Issue 12, pp. 1–21).

1156 <https://doi.org/10.1029/2004JB003241>

1157 Wallace, L. M., & Eberhart-Phillips, D. (2013). *Newly observed , deep slow slip events at the*

1158 *central Hikurangi margin , New Zealand : Implications for downdip variability of slow*

1159 *slip and tremor , and relationship to seismic structure.* 40, 5393–5398.

1160 <https://doi.org/10.1002/2013GL057682>

1161 Wallace, L. M., Fagereng, Å., & Ellis, S. (2012). Upper plate tectonic stress state may infl

1162 uence interseismic coupling on subduction megathrusts. *Geology*, 40(10), 895–898.

1163 <https://doi.org/10.1130/G33373.1>

1164 Wallace, L. M., Reyners, M., Cochran, U., Bannister, S., Barnes, P. M., Berryman, K.,

1165 Downes, G., Eberhart-Phillips, D., Fagereng, A., Ellis, S., Nicol, A., McCaffrey, R.,

1166 Beavan, R. J., Henrys, S., Sutherland, R., Barker, D. H. N., Litchfield, N., Townend, J.,

1167 Robinson, R., ... Power, W. (2009). Characterizing the seismogenic zone of a major

1168 plate boundary subduction thrust: Hikurangi Margin, New Zealand. *Geochemistry,*

1169 *Geophysics, Geosystems*, 10(10). <https://doi.org/10.1029/2009GC002610>

1170 Webb, T. H., & Anderson, H. (1998). Focal mechanisms of large earthquakes in the North

1171 Island of New Zealand: slip partitioning at an oblique active margin. *Geophysical*

1172 *Journal International*, 134, 40–86. <https://doi.org/10.1046/j.1365-246x.1998.00531.x>

1173 White, A. J., Traugott, M. O., & Swarbrick, R. E. (2002). The use of leak-o ff tests as means

1174 of predicting minimum in-situ stress. *Petroleum Geoscience*, 8, 189–193.

1175 <https://doi.org/https://doi.org/10.1144/petgeo.8.2.189>

1176 Wu, H., Chan, C., Shiraiishi, K., Wspanialy, A., & Sugihara, T. (2019). Observed stress state

1177 for the IODP Site C0002 and implication to the stress fi eld of the Nankai Trough

1178 subduction zone. *Tectonophysics*, 765(April), 1–10.

1179 <https://doi.org/10.1016/j.tecto.2019.04.017>

1180 Zhang, J., & Yin, S. (2017). *Real-Time Pore Pressure Detection : Indicators and Improved*

1181 *Methods.* 2017(1).

1182 Zoback, M. D. (2007). *Reservoir Geomechanics.* Cambridge University Press.

1183 Zoback, M. D., Barton, C. A., Brudy, M., Castillo, D. A., Finkbeiner, T., Grollmund, B. R.,

1184 Moos, D. B., Peska, P., Ward, C. D., & Wiprut, D. J. (2003). Determination of stress

1185 orientation and magnitude in deep wells. *International Journal of Rock Mechanics and*

1186 *Mining Sciences*, 40(7–8), 1049–1076. <https://doi.org/10.1016/j.ijrmmms.2003.07.001>

1187

1188 Indo-Pacific Energy (NZ) Ltd. (2002). Waingaromia-2 Well Completion Report, Ministry of
1189 Economic Development New Zealand, Unpublished Open file Petroleum Report 2767.
1190 Tap Oil Limited. (2004). Tawatawa-1 Well Completion Report, Ministry of Economic
1191 Development New Zealand, Unpublished Open file Petroleum Report 3067.
1192 Western Energy New Zealand. (1999), Tuhara-1A Well Completion Report, PEP 38329,
1193 Ministry of Economic Development New Zealand, Unpublished Open file Petroleum
1194 Report 2470.
1195 Western Energy New Zealand. (2001), Well Completion Report Kauhauroa-4B, Ministry of
1196 Economic Development New Zealand, Unpublished Open file Petroleum Report 2610.
1197

Figure 1.

Figure 2.

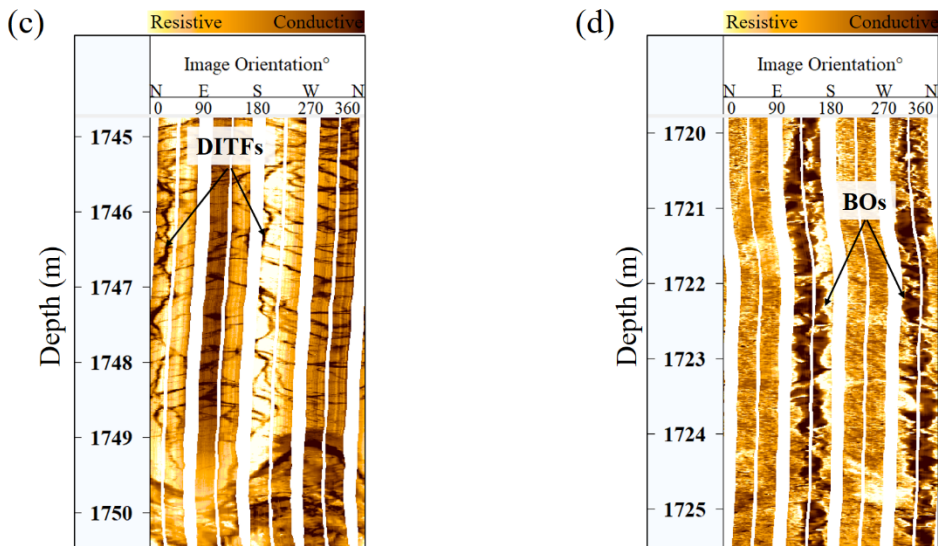
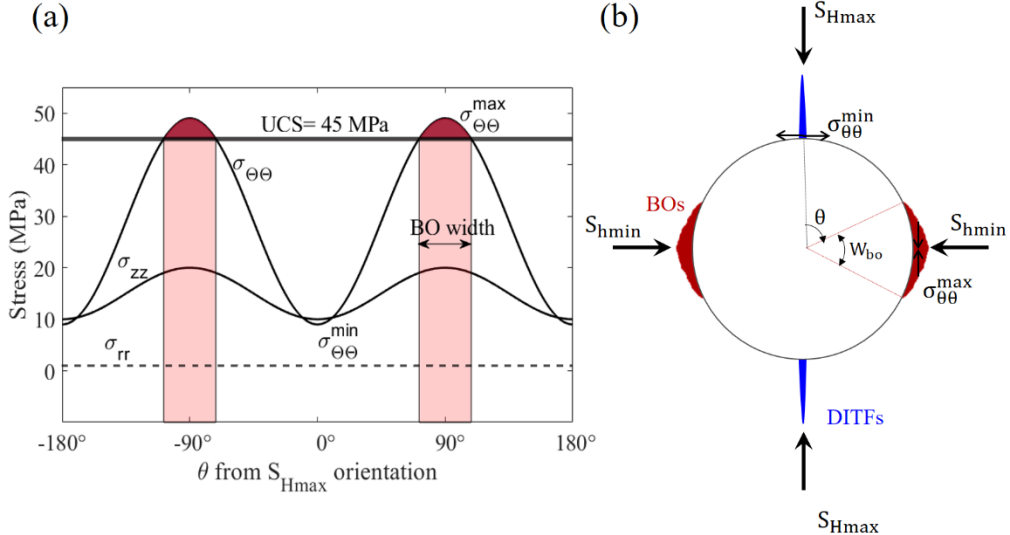


Figure 3.

Tuhara-1A

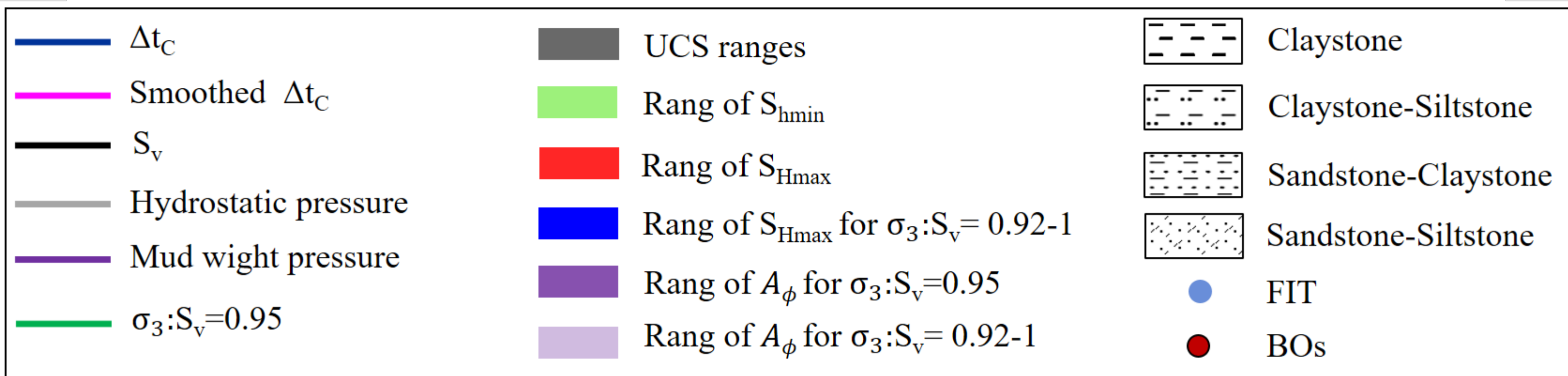
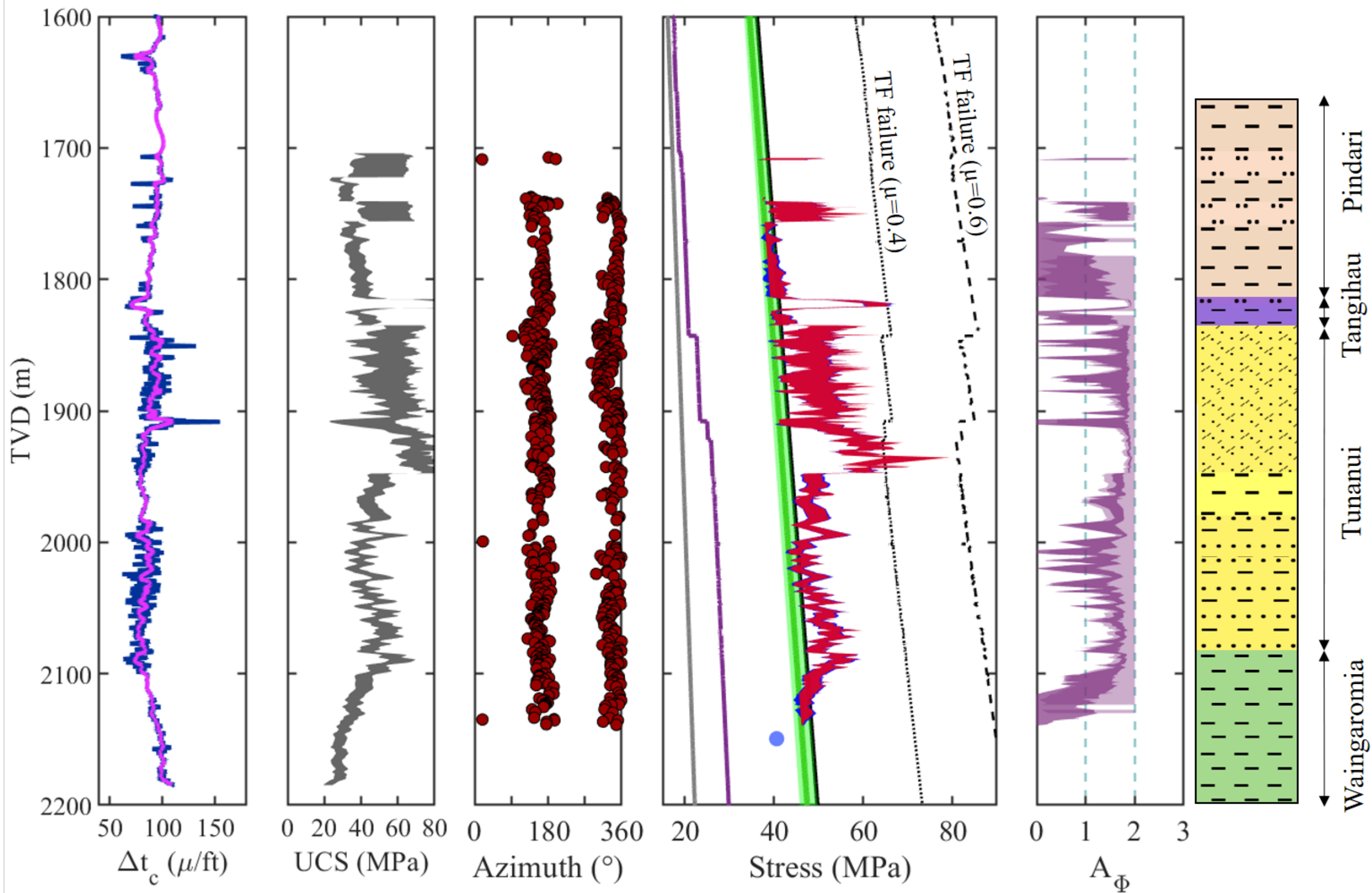


Figure 4.

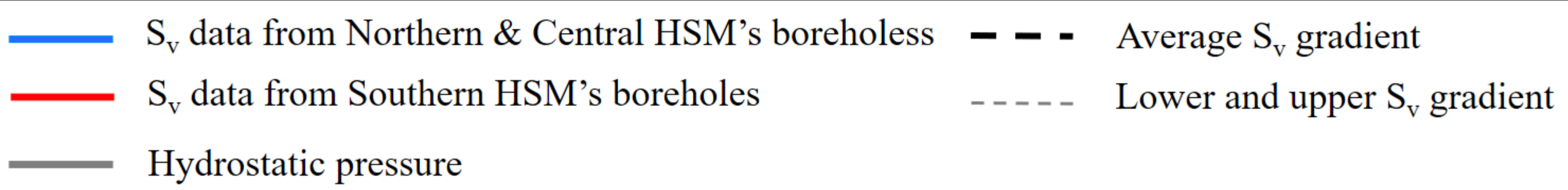
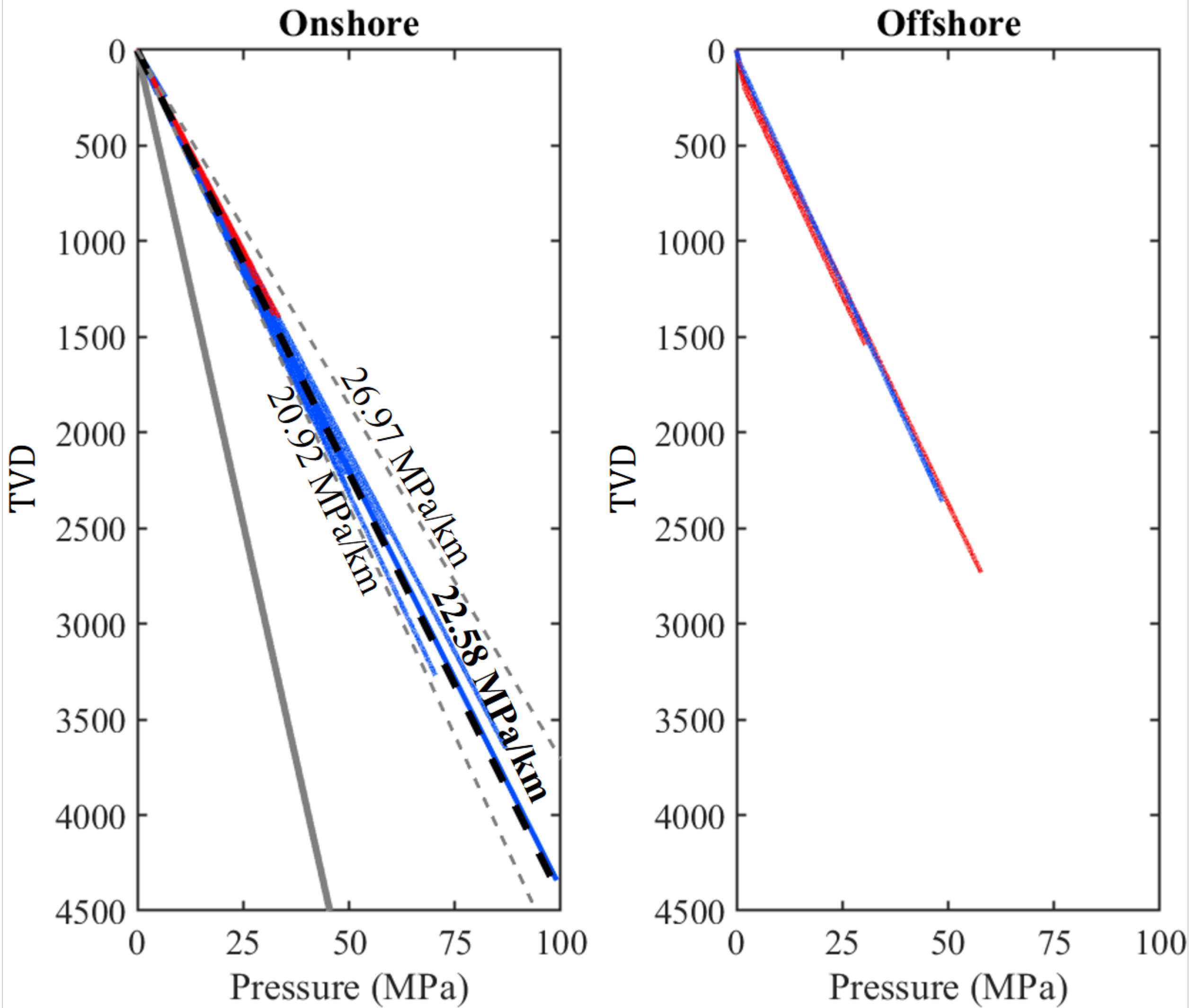
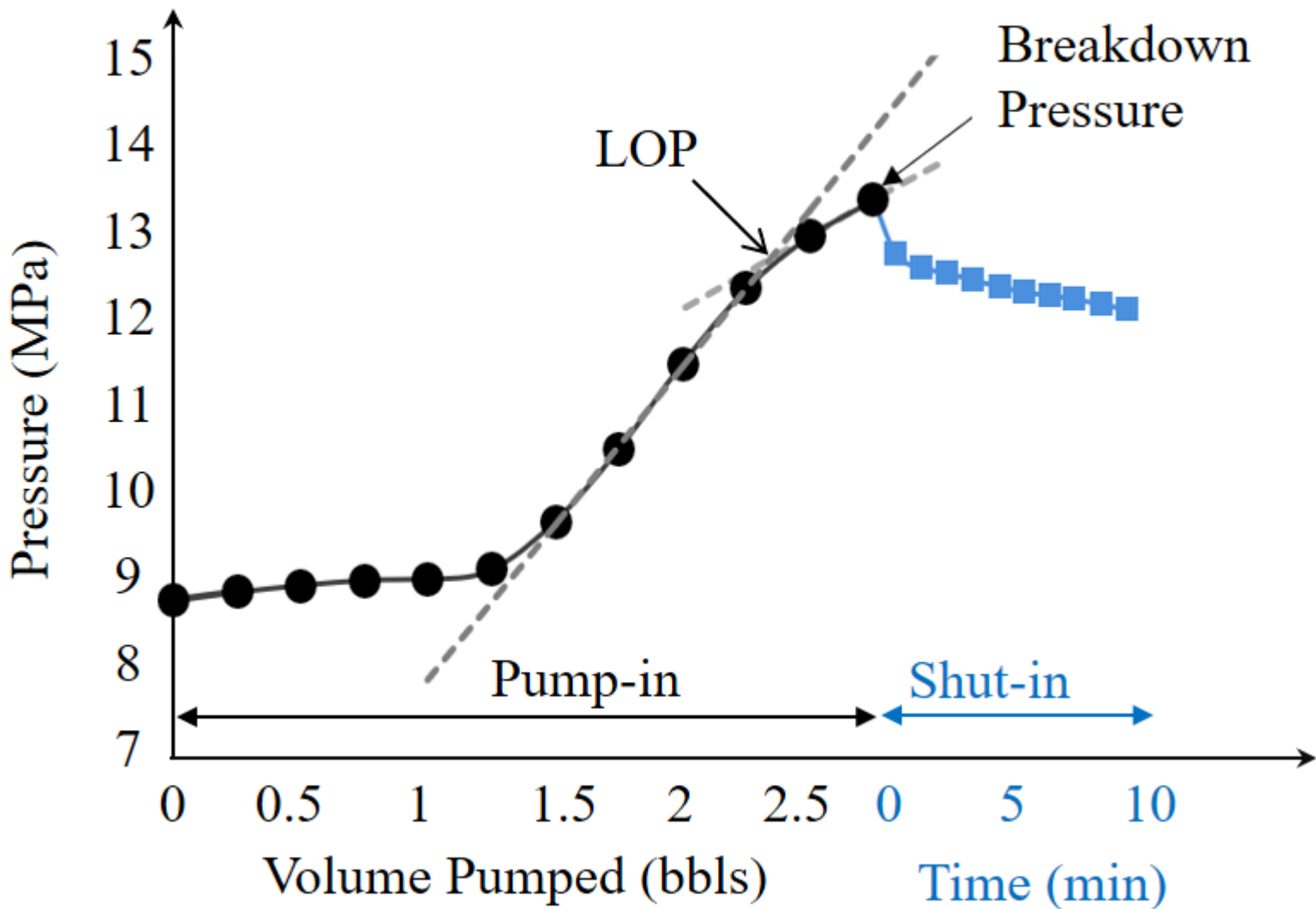


Figure 5.



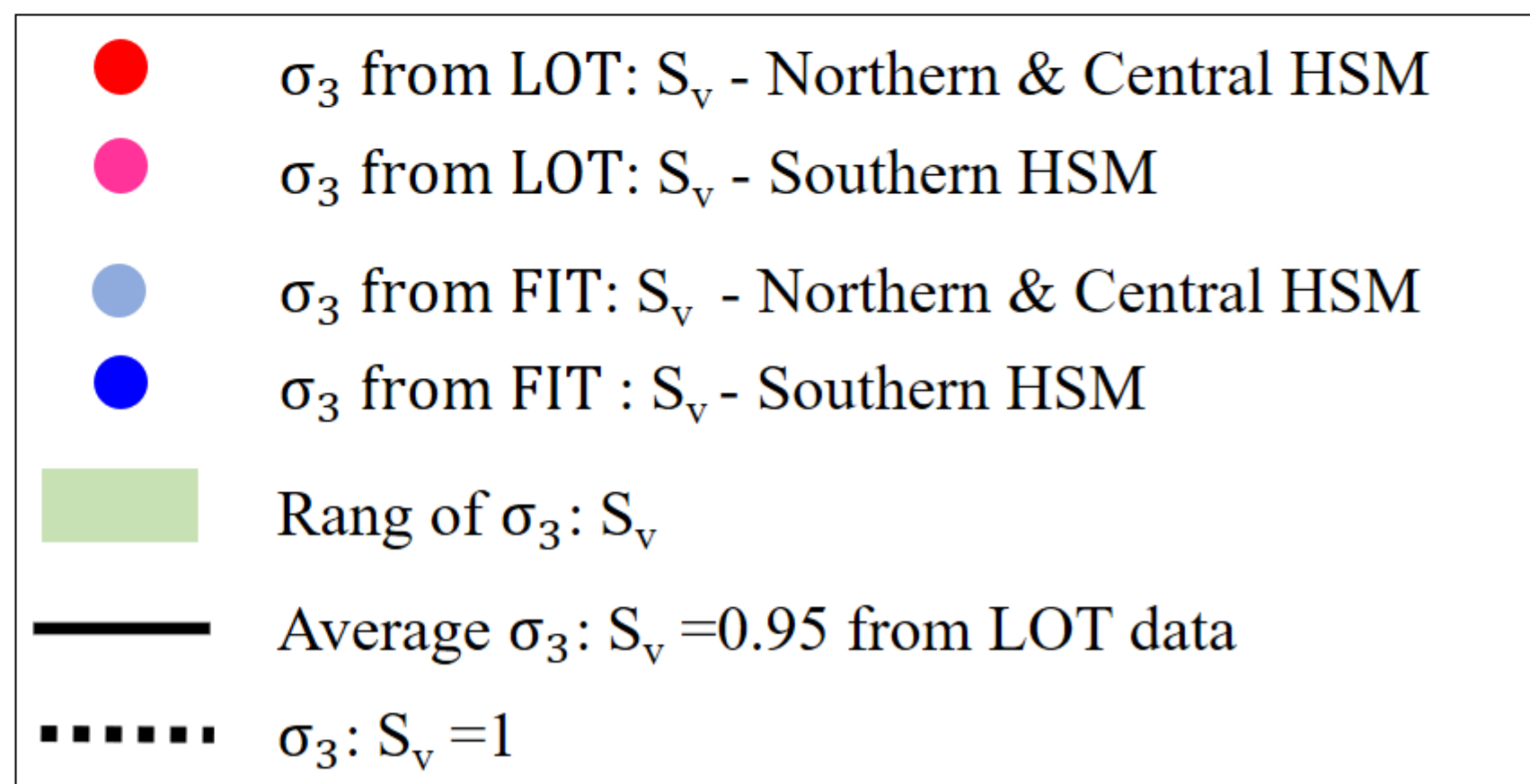
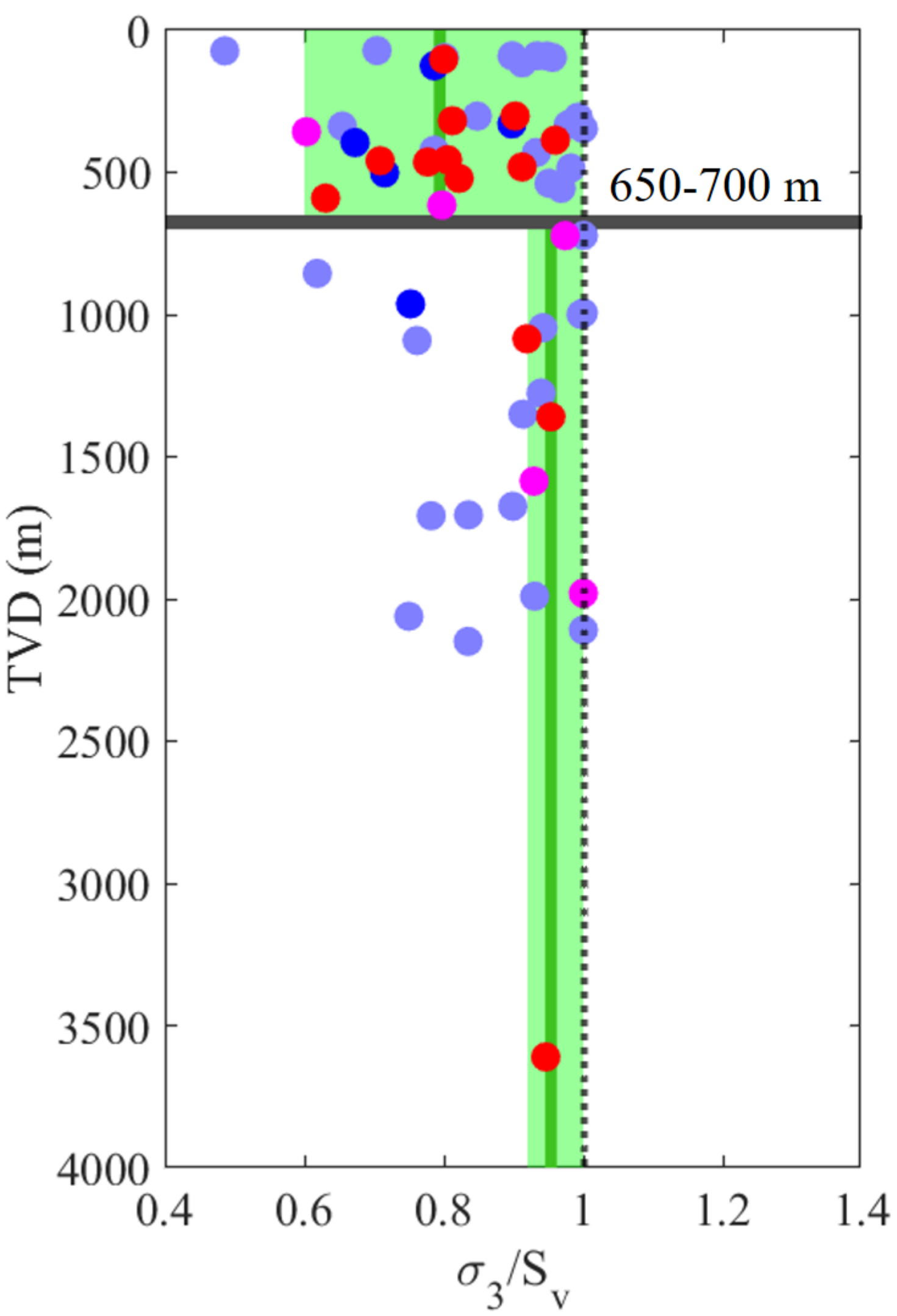


Figure 7.

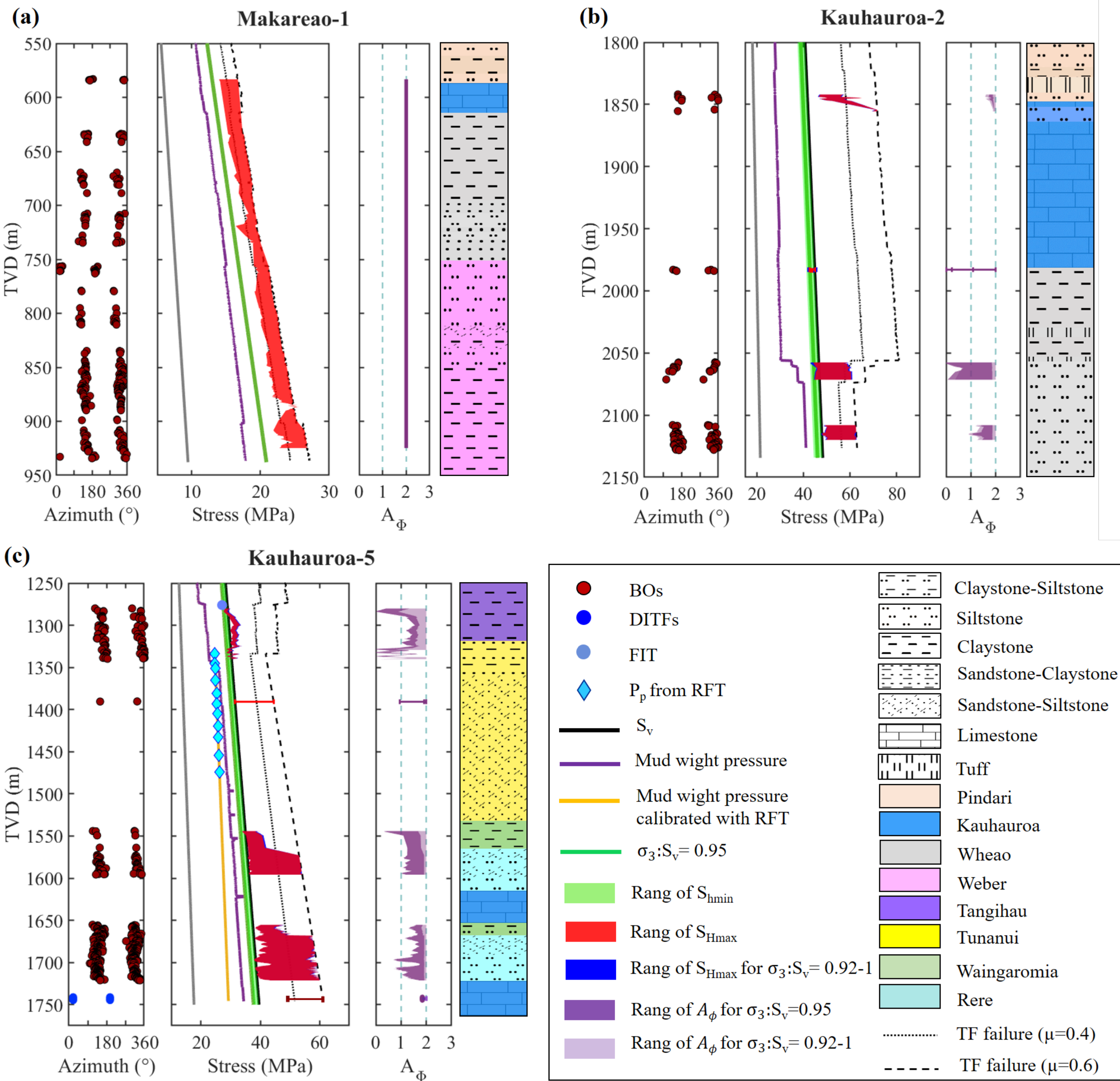


Figure 8.

Kauhauroa-5

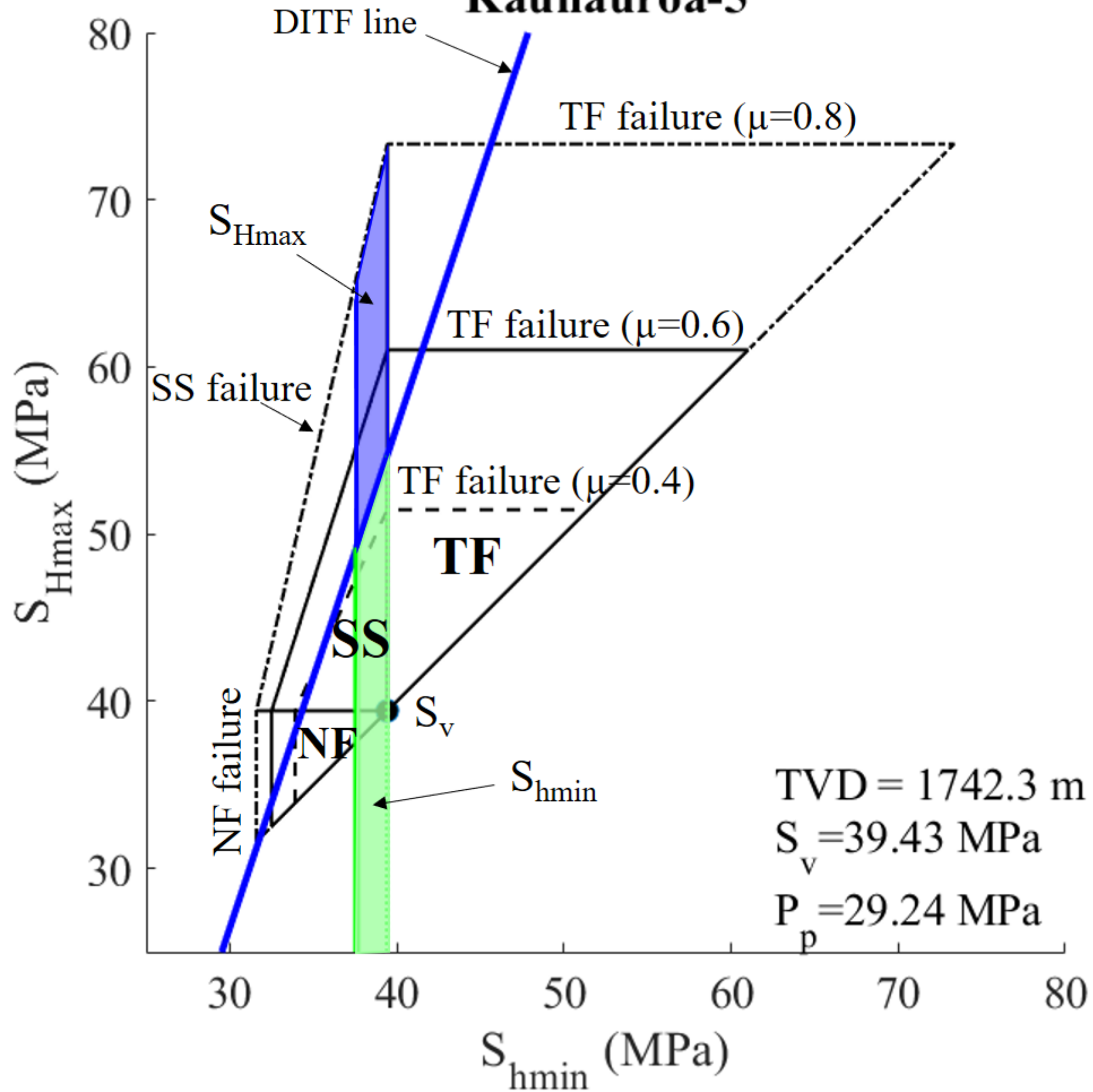


Figure 9.

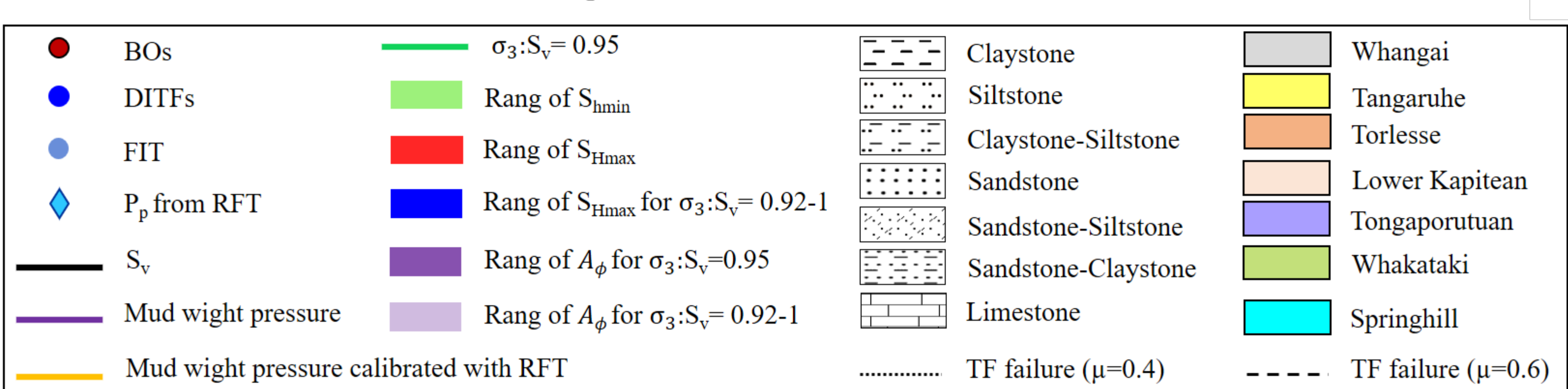
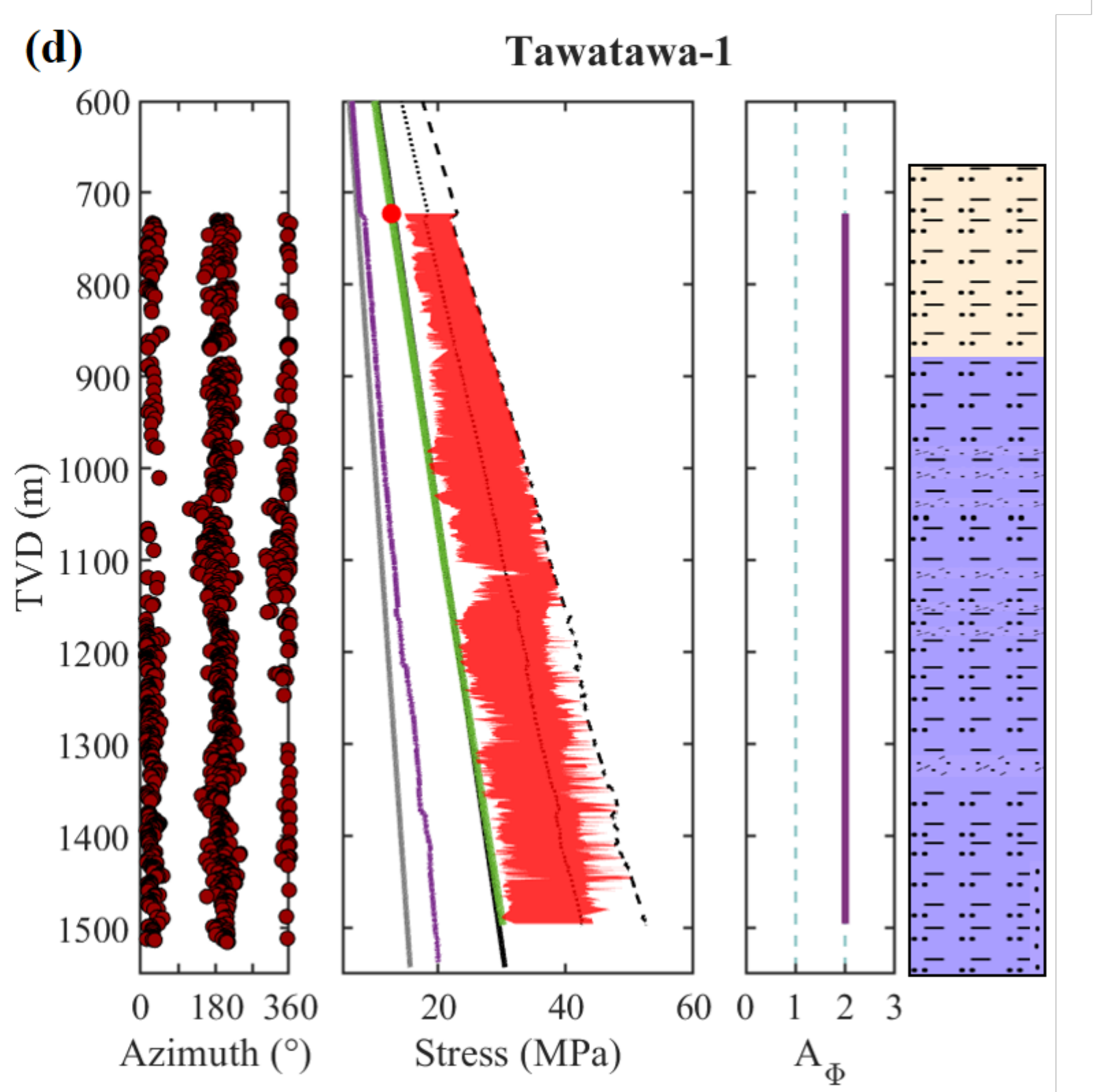
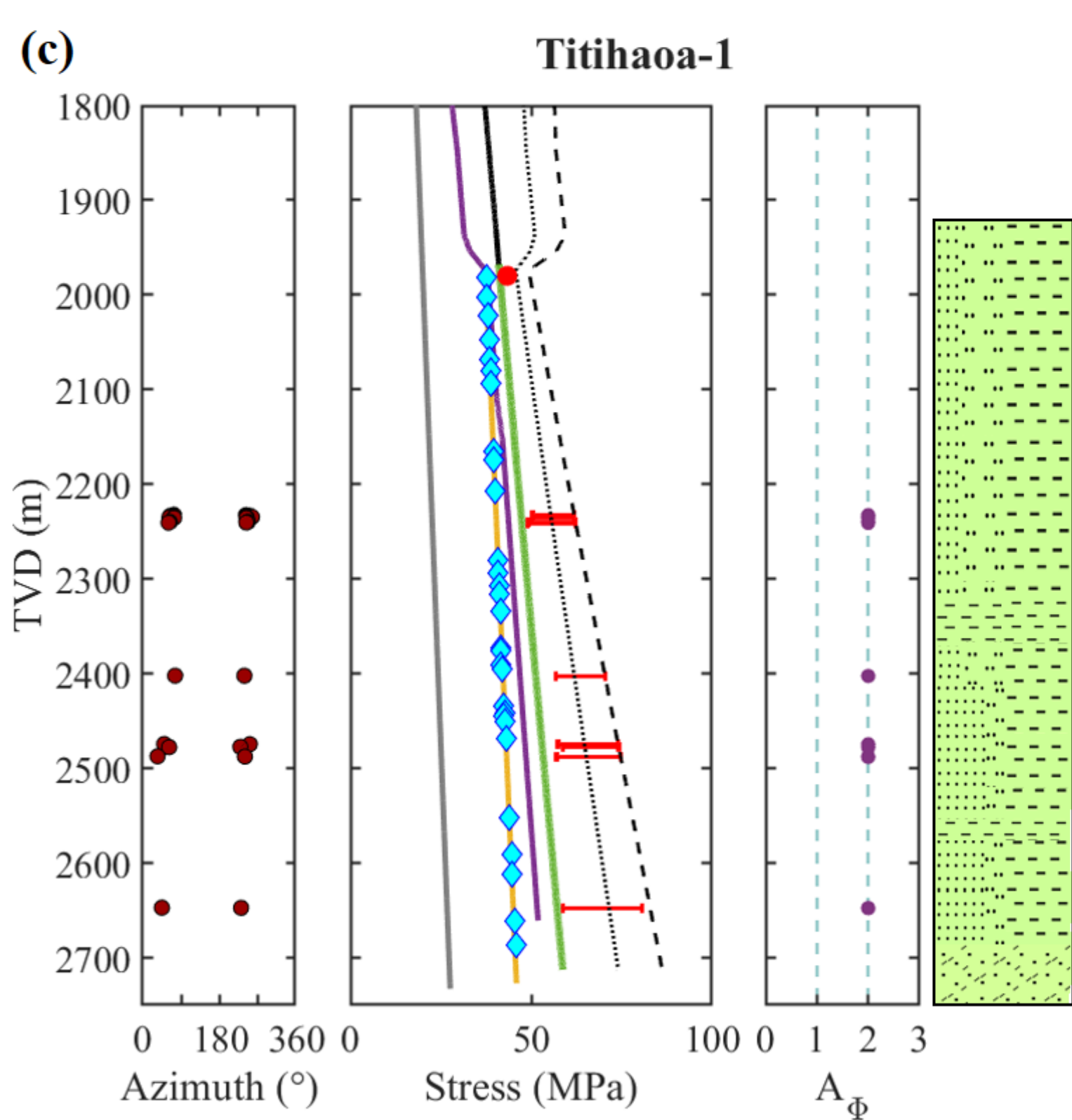
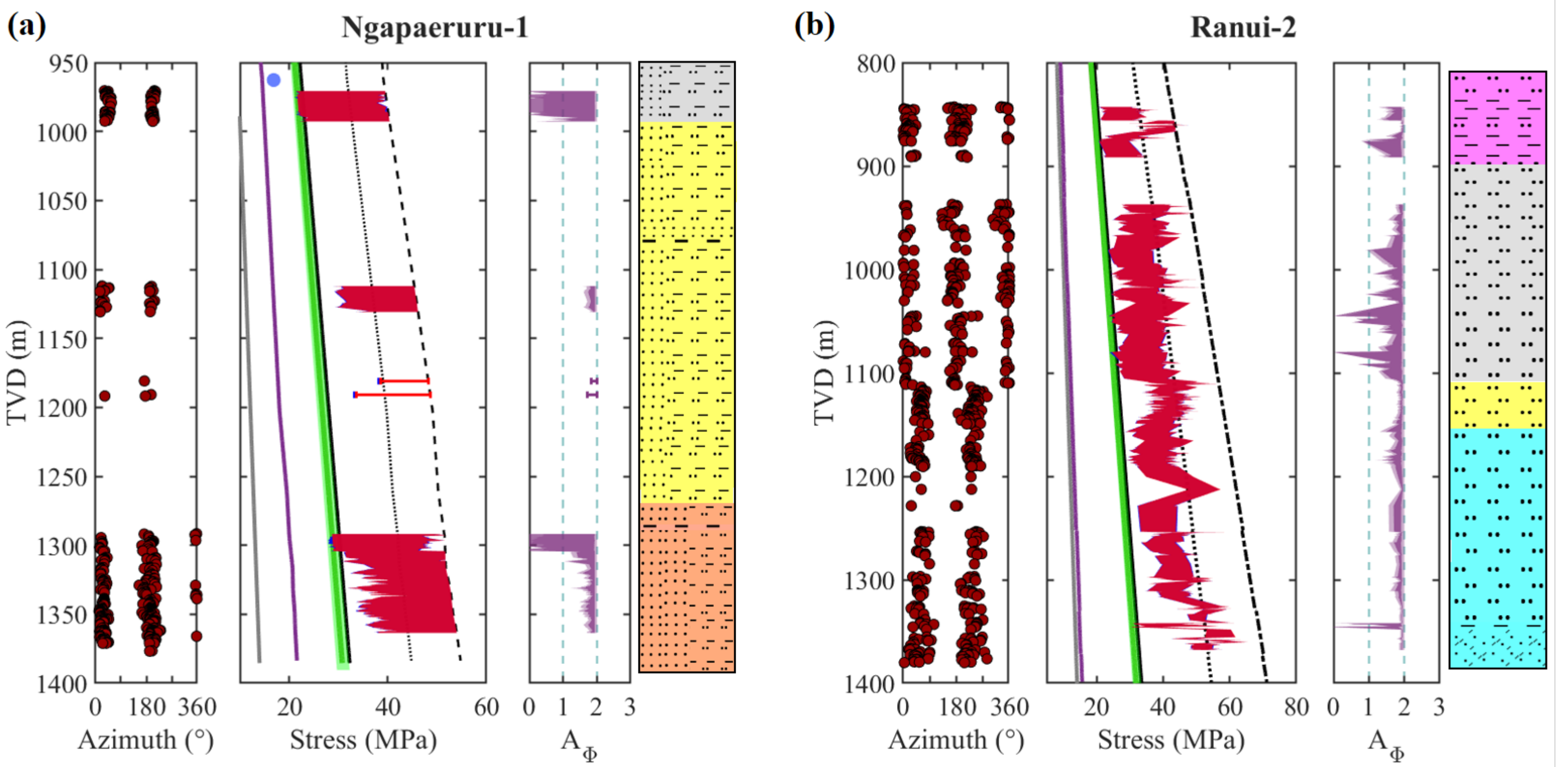


Figure 10.

